Forming short period sub-stellar companions in 47 Tucanae - II. Analytical expressions for the orbital evolution of planets in dense environments

Winter, A.J.; Clarke, C.J.; Rosotti, G.; Giersz, M.

MNRAS 000, 1–29 (2021) Preprint 29 June 2022 Compiled using MNRAS LATEX style file v3.0

Forming short period sub-stellar companions in 47 Tucanae – II. Analytic expressions for the orbital evolution of planets in dense environments

Andrew J. Winter,[1,2,3]★ Cathie J. Clarke[3], Giovanni Rosotti[2,4], Mirek Giersz[5]
[1]Zentrum für Astronomie, Heidelberg University, Albert Ueberle Str. 2, 69120 Heidelberg, Germany
[2]School of Physics and Astronomy, University of Leicester, Leicester, LE1 7RH, UK
[3]Institute of Astronomy, University of Cambridge, Madingley Road, Cambridge, CB3 0HA, UK
[4]Leiden Observatory, Leiden University, P.O. Box 9513, NL-2300 RA Leiden, the Netherlands
[5]Nicolaus Copernicus Astronomical Center, Polish Academy of Sciences, ul. Bartycka 18, Warsaw 00-716 Poland

Accepted Xxxxx XX. Received Xxxxx XX; in original form 2019 April XX

ABSTRACT

Short period, massive planets, known as hot Jupiters (HJs), have been discovered around ∼ 1 percent of local field stars. The inward migration necessary to produce HJs may be 'low eccentricity', due to torques in the primordial disc, or 'high eccentricity' (HEM). The latter involves exciting high orbital eccentricity, allowing sufficiently close passages with the host star to raise circularising tides in the planet. We present an analytic framework for quantifying the role of dynamical encounters in high density environments during HEM. We show that encounters can enhance or suppress HEM, depending on the local stellar density and the initial semi-major axis a_0. For moderate densities, external perturbations can excite large eccentricities that allow a planet to circularise over the stellar lifetime. At extremely high densities, these perturbations can instead result in tidal disruption of the planet, thus yielding no HJ. This may explain the apparent excess of HJs in M67 compared with their local field star abundance versus their apparent deficit in 47 Tuc. Applying our analytic framework, we demonstrate that for an initial massive planet population similar to the field, the expected HJ occurrence rate in 47 Tuc is $f_{\rm HJ} = 2.2 \times 10^{-3}$, which remains consistent with present constraints. Future large (sample sizes $\gtrsim 10^5$) or sensitive transit surveys of stars in globular clusters are required to refute the hypothesis that the initial planet population is similar to the solar neighbourhood average. Non-detection in such surveys would have broad consequences for planet formation theory, implying planet formation rates in globular clusters must be suppressed across a wide range of a_0.

Key words: planets and satellites: formation, dynamical evolution and stability, gaseous planets – stars: kinematics and dynamics – globular clusters: individual: 47 Tuc

1 INTRODUCTION

Hot Jupiters (HJs) are gas giant planets on short orbital periods ($\lesssim 10$ days) and are the class of planet to which the first discovered planet belongs (51 Peg b – Mayor & Queloz 1995). They remain over-represented among known exoplanets with respect to their occurrence rates, mainly due to their comparatively high detection efficiency among both transit and radial velocity surveys. A great deal of planet formation theory has been devoted to understanding their formation (for recent reviews, see Dawson & Johnson 2018; Fortney et al. 2021). Mass budget constraints imply the the majority of the mass of the HJ must be accreted outside of the current orbits, thus one of the main questions regarding their formation is how they migrated inwards.

Broadly, the possible mechanisms for migration of HJs can be divided into two categories, labelled 'low eccentricity migration' (LEM) and 'high eccentricity migration' (HEM). In LEM, massive planets move inwards as a consequence of torques within the protoplanetary disk in which they form (e.g. Goldreich & Tremaine 1980; Lin & Papaloizou 1986; Lin et al. 1996). In order to produce HJs, this requires efficient 'type II' migration, operating once a gap in the gas surface density profile has opened. Current evidence suggests low viscosity in protoplanetary discs (e.g. Pinte et al. 2016; Trapman et al. 2020), which would imply slow type II migration rates (Lega et al. 2021). While this does not categorically rule out such a formation scenario, evidence for HJs around stars younger than ∼ 600 Myr remains scarce (Paulson & Yelda 2006; Bailey et al. 2018; Takarada et al. 2020), with younger candidates often the topic of debate – e.g. around CI Tau (Donati et al. 2020) and V830 Tau (Damasso et al. 2020).

On the other hand, HEM represents a later mode of migration, relying on close passages with the host star and orbital circularisation due to tides raised at periastron (e.g. Goldreich & Soter 1966; Hut 1981; Adams & Laughlin 2006). The necessary eccen-

★ andrew.winter@uni-heidelberg.de

tricities may be excited by oscillations during interaction with an outer companion (Kozai-Lidov – Kozai 1962; Lidov 1962; Naoz 2016; Hamers & Lai 2017; Fontanive et al. 2019; Belokurov et al. 2020) or by dynamical instability within a planetary system (Rasio & Ford 1996; Carrera et al. 2019). Either of these scenarios may originate from the initial properties of the system (for example, see Pu & Wu 2015 versus Yee et al. 2021), or be due to perturbation by neighbouring stars in stellar clusters (Bonnell et al. 2001; Shara et al. 2016; Brucalassi et al. 2016; Li et al. 2020; Winter et al. 2020; Rodet et al. 2021; Wang et al. 2022). In favour of HEM as the origin of at least some HJs, Dong et al. (2021) recently discovered a planet of mass $\sim 5\,M_{\rm J}$, TOI-3362b, that appears to be undergoing tidal circularisation. Statistically, the obliquity distribution of HJs appears consistent with late tidal damping after HEM (Rice et al. 2022). Meanwhile, free-floating planets have recently been found to be abundant in the young Upper Scorpius association (Miret-Roig et al. 2021), suggesting that a significant fraction of planetary systems have undergone chaotic dynamical decay. Finally, systems that have not undergone dynamical decay appear consistent with Hill radius limited growth within a protoplanetary disc, which suggests inefficient type II migration (Winter & Alexander 2021).

Disentangling the (dominant) formation pathway for HJs requires correlating their occurrence rates with the properties of their host star. This includes intrinsic properties of the host star, such as stellar mass and metallicity (e.g. Santos et al. 2001; Boss 2002; Johnson et al. 2010), but also the external environment. This was the motivation of Gilliland et al. (2000, hereafter GBG+00) in carrying out a *Hubble Space Telescope* survey of the globular cluster 47 Tuc for short period massive planets. The non-detection of any transit signal among 34, 091 stars was initially thought to put upper limits on the HJ occurrence being $\lesssim 0.2$ percent, significantly fewer than the solar neighbourhood average (1.2 ± 0.4 percent inferred from RV surveys – Wright et al. 2012). However, Masuda & Winn (2017) applied an updated distribution of known HJ properties to demonstrate that the number of HJs in the GBG+00 sample would be $2.2^{+1.6}_{-1.1}$ if the planet population is indistinguishable to those hosted by *Kepler* stars of similar masses. The result may therefore be less significant than initially thought. This also applies to the wide field search for HJs by Weldrake et al. (2005). Whether or not HJs exist in 47 Tuc in comparable numbers to the field therefore remains an open question.

If HJ formation is suppressed in 47 Tuc relative to the field, this could originate from lower formation rates due to the lower metallicity (Santos et al. 2001; Boss 2002; Ercolano & Clarke 2010) or external irradiation of the planet forming disc by strong ultraviolet fields (Johnstone et al. 1998; Adams et al. 2004; Facchini et al. 2016; Winter et al. 2018b; Haworth et al. 2018). The influence of external UV fields on giant planet occurrence remains uncertain, both empirically and theoretically. However, in terms of metallicity, Johnson et al. (2010) estimated a scaling of occurrence rates of HJs as $10^{1.2\,[{\rm Fe/H}]}$, corresponding to approximately an order of magnitude for metallicity of 47 Tuc, with $[{\rm Fe/H}] \approx -0.7$, with respect to the *Kepler* field with $[{\rm Fe/H}] \approx 0$. Due to the small number of stars with low metallicity in the *Kepler* field, this dependence remains challenging to constrain with *Kepler* data (see dicussion by Masuda & Winn 2017). It is also unclear whether metallicity is a fundamental property that determines giant planet occurrence, or whether it is an extraneous property that correlates via formation conditions.

Despite the above considerations, the apparent absence of HJs found in 47 Tuc may remain surprising within the paradigm of HEM. A naive expectation would be that if any planets at all exist in globular clusters then they should be more likely, not less likely, to undergo dynamical perturbation with subsequent circularisation. Such a trend has been hinted at by the marginally significant overabundance of HJs in the dense cluster M67 (Brucalassi et al. 2016). Quantifying this expectation and reconciling the tension between the findings in M67 and 47 Tuc partially motivates this work.

In this, the second of a two paper mini-series, we consider the formation of HJs in 47 Tuc by HEM. We apply a Monte Carlo model for the dynamical evolution of 47 Tuc, introduced in Paper I (Winter et al. 2022), to follow the rate at which migrating planets undergo dynamical perturbation, interpreting this rate in terms of the efficiency of HJ production. The analysis presented in this work is complementary to that of Hamers & Tremaine (2017, hereafter HT17), who performed numerical simulations to show how the formation of HJs varies with stellar density due to encounters within some radius $R_{\rm enc}$. In this work, we offer a theoretical framework to interpret these results, allowing us to generalise the findings across a wide parameter space pertaining to both the properties of the star-planet system and external environment. Coupled with a dynamical model, our analytic prescription allows us to quantify the probabilities of various outcomes for planetary systems over the lifetime of 47 Tuc.

The remainder of this manuscript is organised as follows. We consider the theoretical rates of tidal circularisation and dynamical perturbations in Section 2. We apply our results in terms of the dynamical model for 47 Tuc in Section 3, wherein we also make predictions for future surveys. We summarise our conclusions in Section 4.

2 ORBITAL EVOLUTION THEORY

2.1 Overview

2.1.1 Motivation

While the cause of the inward migration of HJs remains uncertain (e.g. Fortney et al. 2021, for a recent review), we will here assume that gas giants on short orbital periods are produced by some dynamical perturbation of the initial formation configuration (e.g Rasio & Ford 1996; Ford & Rasio 2008; Carrera et al. 2019; Winter & Alexander 2021; Miret-Roig et al. 2021), rather than from efficient migration within a stellar disc (e.g. Lin et al. 1996; Baruteau et al. 2014). Such a dynamical perturbation can result in a sufficiently high eccentricity to yield close passages with the central star and tidal exchanges that shrink and circularise the orbit (e.g. Hut 1981; Eggleton et al. 1998; Jackson et al. 2008). In this work, we consider how orbital perturbations due to stellar encounters influence a circularising planet.

2.1.2 Approach

In this section, we aim to produce an analytic estimate for various possible outcomes for a planet evolving in a high density environment. To this end, in Section 2.2 we first discuss the theoretical tidal ciricularisation rate. Circularisation occurs due to close passages of the planet with the host star, during which the tides raised in the planet reduce its orbital energy and shrink the orbit while conserving the semi-latus rectum l.

We then quantify the changes of the orbital eccentricity due to encounters in a dense stellar environment. Such encounters can change how a planet circularises, possibly curtailing migration by

reducing the eccentricity or inducing tidal disruption due to extremely close passages with the host star. We consider the encounter-driven evolution of eccentricity, rather than semi-major axis, for two reasons. Firstly, because the rate of circularisation for a planet on an highly eccentric orbit is strongly influenced by small changes in eccentricity. Secondly, because the change of angular momentum due to a stellar encounter scales as a power-law in closest approach distance r_p (Heggie & Rasio 1996). On the other hand, changes in energy become exponentially smaller with increasing r_p (Heggie 1975). Thus the most common encounters, those occurring with large r_p, predominantly alter eccentricity.

In Section 2.3 we quantify the cross section for perturbations by a neighbouring star in terms of a small change in eccentricity ϵ. We convert this to a rate of perturbation given a local stellar density and velocity dispersion in Section 2.4. We discuss the interpretation of these perturbation rates in Section 2.5. We then apply the perturbation rates to quantify the statistical evolution of orbital eccentricity due to stellar encounters in Section 2.6.

Finally, we consider how dynamical perturbation influences tidal circularisation outcomes. In the first instance, we make arguments on the maximum possible l along which a planet can circularise in Section 2.7. This is set by the condition that the perturbation rate balances with the circularisation rate. We then compare these analytic predictions to a numerical experiment in Section 2.8. This allows us to interpret the fraction of tidally destroyed planets, which have a minimum pericentre distance that is too close to their host star to survive (Section 2.9). We additionally consider the rate of ionisation of a planetary system in Section 2.10. With these calculations, in Section 2.11 we establish the analytic framework for computing the relative outcome probabilities, with comparisons to the previous numerical experiments of HT17. We apply this framework to 47 Tuc in Section 3.

2.2 Pseudo-synchronous tidal circularisation rate

In order to understand how eccentricity perturbations alter the evolution of a would-be HJ, we first need to estimate the circularisation rates. We will assume that the dissipation of orbital energy is dominated by tides raised in the planet, and that we are in the limit of low obliquity (although see also Alexander 1973). In this case, the basic equations for the long term semi-major axis and eccentricity evolution of a planet circularising by successive close approaches with its host star are given by Hut (1981):

$$\dot{a}_\mathrm{tide} = -6k_\mathrm{p}\tau_\mathrm{p}n^2q^{-1}\left(\frac{R_\mathrm{p}}{a}\right)^5\frac{a}{(1-e^2)^{15/2}}\times \\ \times\left\{f_1(e^2)-(1-e^2)^{3/2}f_2(e^2)\frac{\Omega_\mathrm{p}}{n}\right\} \quad (1)$$

$$\dot{e}_\mathrm{tide} = -27k_\mathrm{p}\tau_\mathrm{p}n^2q^{-1}\left(\frac{R_\mathrm{p}}{a}\right)^5\frac{e}{(1-e^2)^{13/2}}\times \\ \times\left\{f_3(e^2)-\frac{11}{18}(1-e^2)^{3/2}f_4(e^2)\frac{\Omega_\mathrm{p}}{n}\right\} \quad (2)$$

$$\dot{\Omega}_\mathrm{p,tide} = 3k_\mathrm{p}\tau_\mathrm{p}n\frac{q^{-2}}{r_\mathrm{g}^2}\left(\frac{R_\mathrm{p}}{a}\right)^6\frac{1}{(1-e^2)^6}\times \\ \times\left\{f_2(e^2)-(1-e^2)^{3/2}f_5(e^2)\frac{\Omega_\mathrm{p}}{n}\right\} \quad (3)$$

where Ω_p is the angular frequency of the rotating planet, r_g is the radius of gyration and

$$n = \sqrt{\frac{Gm_*(1+q)}{a^3}}, \quad (4)$$

while R_p, k_p, and τ_p are the planetary radius, apsidal motion constant, and tidal time lag. We will generally follow HT17 in adopting $k_\mathrm{p} = 0.25$ and $\tau_\mathrm{p} = 0.66$ s, while we fix $R_\mathrm{p} = 0.1\,R_\odot$. The functions f_i are defined:

$$f_1(e^2) = 1+\frac{31}{2}e^2+\frac{55}{8}e^4+\frac{185}{16}e^6+\frac{25}{64}e^8 \quad (5)$$

$$f_2(e^2) = 1+\frac{15}{2}e^2+\frac{45}{8}e^4+\frac{5}{16}e^6 \quad (6)$$

$$f_3(e^2) = 1+\frac{15}{4}e^2+\frac{15}{8}e^4+\frac{5}{64}e^6 \quad (7)$$

$$f_4(e^2) = 1+\frac{3}{2}e^2+\frac{1}{8}e^4 \quad (8)$$

$$f_5(e^2) = 1+3e^2+\frac{3}{8}e^4. \quad (9)$$

This set of equations dictates the tidal evolution of a low obliquity planet.

In principle, one then must now choose an initial orbital frequency for the planet, as well as semi-major axis and eccentricity, to solve the system of equations 1–3. Indeed, in the parabolic limit $e \to 1$, this choice can dictate the outcome due to the tidal force on the planet orbit, where if the initial orbital frequency $\Omega_{\mathrm{p},0}$ exceeds a critical value then the planet will escape rather than circularise (Hut 1982). However, we expect that the rotational angular momentum of the planet is much smaller than its orbital angular momentum, which justifies the assumption that the orbitally averaged tidal torque is zero. This is equivalent to the pseudo-synchronisation condition $\dot{\Omega}_\mathrm{p} \approx 0$, or:

$$\Omega_\mathrm{p} \approx n\frac{f_2(e^2)}{(1-e^2)^{3/2}f_5(e^2)}. \quad (10)$$

This can be compared directly to equation 42 of Hut (1981, also the prescription of HT17). One can then rewrite equations 1 and 2:

$$\dot{a}_\mathrm{tide} = -21k_\mathrm{p}\tau_\mathrm{p}n^2q^{-1}\left(\frac{R_\mathrm{p}}{a}\right)^5\frac{ae^2f(e^2)}{(1-e^2)^{15/2}} \quad (11)$$

$$\dot{e}_\mathrm{tide} = -\frac{21}{2}k_\mathrm{p}\tau_\mathrm{p}n^2q^{-1}\left(\frac{R_\mathrm{p}}{a}\right)^5\frac{ef(e^2)}{(1-e^2)^{13/2}}, \quad (12)$$

where

$$f(e^2) = \frac{1+\frac{45}{14}e^2+8e^4+\frac{685}{224}e^6+\frac{255}{448}e^8+\frac{25}{1792}e^{10}}{1+3e^2+\frac{3}{8}e^4}. \quad (13)$$

From equations 11 and 12 it is clear that a circularising planet that is slowly rotating always preserves the semi-latus rectum (SLR) $l = a(1-e^2)$, or equivalently the specific angular momentum $h \propto \sqrt{l}$.

2.3 Perturbation cross section

We must now quantify the rate at which the eccentricity of an orbiting planet is altered by encounters with other stars. Any random (uncorrelated) dynamical encounter between stars can be expressed in terms of the effective cross section. This cross section is the effective area 'seen' by neighbouring stars in a given environment, averaged over all possible orientations. In this case, we are interested in any perturbation that results in a significant change in the orbit of the planet. The distinction here compared to previous studies investigating perturbations of planetary systems by stellar flyby, is that we are not initially concerned by whether the planet is subsequently lost from the system (cf. Hills & Dissly 1989; Davies & Sigurdsson 2001; Bonnell et al. 2001; Fregeau et al. 2006, for example). High eccentricity migration requires close passage of the migrating planet within a few stellar radii of the host star over the entire circularisation time-scale $\tau_{\rm circ}$. Thus, even slight external perturbations to the orbit may alter the migration rate. The closest approach of an external perturber required in this case may therefore be far larger than for ionisation (or tidal capture – cf. Paper I).

2.3.1 *Parabolic encounters*

Heggie & Rasio (1996) estimated the angle-averaged effective cross section for perturbation of the eccentricity $|\epsilon|$ greater than some threshold eccentricity $\epsilon_{\rm thr}$ of a binary with primary mass m_*, mass ratio q, initial semi-major axis a_0, eccentricity e_0 (their equation 19). This approximation is made by considering tidal and slow encounters, including only the quadrupole terms and taking the first order change in eccentricity:

$$\epsilon \approx \frac{\delta \boldsymbol{e} \cdot \boldsymbol{e}_0}{|\boldsymbol{e}_0|}, \tag{14}$$

where $\boldsymbol{e}_0$ is the original eccentricity vector of the binary and $\delta \boldsymbol{e}$ is the change in this vector post-encounter. In the gravitationally focused limit, the cross section for interaction with a star of mass $m_{\rm pert}$ with relative velocity at infinite separation v_∞ can be written (see Heggie & Rasio 1996):

$$\begin{aligned}\sigma_{\rm pert}^{\rm (foc)} &\approx 2 \cdot \frac{9\sqrt{3}}{14\pi}\left(\frac{15\pi}{4}\right)^{2/3}\left[\Gamma\left(\frac{2}{3}\right)\Gamma\left(\frac{5}{6}\right)\right]^2 \times \\ &\times \left(\frac{m_{\rm pert}^2}{(1+q)m_* m_{\rm tot}}\right)^{1/3} \frac{G m_{\rm tot} a_0}{v_\infty^2} e_0^{2/3}(1-e_0^2)^{1/3}\epsilon_{\rm thr}^{-2/3} \\ &= C_{\rm foc} \cdot \pi a_0^2 \cdot \epsilon_{\rm thr}^{-2/3} y^{2/3}\left(\frac{v_\infty}{v_{\rm orb}}\right)^{-2}\left[1+q_{\rm pert}\right], \end{aligned} \tag{15}$$

where $C_{\rm foc} \approx 2.73$ is a dimensionless constant and

$$q_{\rm pert} = \frac{m_{\rm pert}}{(1+q)m_*}. \tag{16}$$

We have defined:

$$y \equiv e_0\sqrt{1-e_0^2}\,\frac{m_{\rm pert}}{\sqrt{(1+q)m_* m_{\rm tot}}}, \tag{17}$$

the planet orbital velocity is

$$v_{\rm orb} = \sqrt{\frac{G m_*(1+q)}{a_0}}, \tag{18}$$

the total mass of the whole system is $m_{\rm tot} = m_*(1+q) + m_{\rm pert}$ and we include the first factor 2 in the first expression of equation 15 because we initially do not care if δe is positive or negative.

2.3.2 *Hyperbolic encounters*

Equation 15 is derived assuming that the encounter is gravitationally focused (the eccentricity of the perturbing star is $e_{\rm pert} \approx 1$). However, in our context the three-dimensional velocity dispersion in the centre of 47 Tuc exceeds or is comparable to the typical orbital velocity $v_{\rm orb} \sim 10\,{\rm km\,s^{-1}}$ (see Paper I) and this may yield $e_{\rm pert} > 1$ for the encounters of interest. The velocity dispersion is therefore too large to assume that focused encounters dominate the overall perturbation rate. The more general expression for ϵ due to a hyperbolic encounter is much less elegant, such that an equivalent of equation 15 must be derived numerically. We review the approach to this problem in Appendix A, where we show that the form of the hyperbolic equivalent of equation 15 is:

$$\sigma_{\rm pert}^{\rm (hyp)} = C_{\rm hyp} \cdot \pi a_0^2 \cdot y \epsilon_{\rm thr}^{-1}\left(\frac{v_\infty}{v_{\rm orb}}\right)^{-1}\sqrt{1+q_{\rm pert}}, \tag{19}$$

where $C_{\rm hyp}$ is another dimensionless constant. The general perturbation cross section can then be approximated:

$$\sigma_{\rm pert} \approx \sigma_{\rm pert}^{\rm (foc)}\left[1 + \Delta_{\rm hf}\frac{v_\infty}{v_{\rm orb}}\right] \tag{20}$$

for

$$\Delta_{\rm hf} = C_{\rm hf} y^{1/3}\epsilon_{\rm thr}^{-1/3}\left[1+q_{\rm pert}\right]^{-1/2}. \tag{21}$$

We have introduced scaling parameter $C_{\rm hf}$, which we infer numerically to be $C_{\rm hf} \approx 0.67$, or equivalently $C_{\rm hyp} = C_{\rm hf} \cdot C_{\rm foc} \approx 1.83$ (see Appendix A).

2.4 Perturbation rate

From the cross sections derived in Section 2.3, we can estimate the perturbation rate $\Gamma_{\rm pert} = \tau_{\rm pert}^{-1}$ for a given local number density $n_{\rm tot}$ of (sub-)stellar objects and velocity dispersion σ_v. The differential rate of perturbation is:

$${\rm d}\Gamma_{\rm pert} = v_\infty\, n_{\rm tot}\, \sigma_{\rm pert}(v_\infty)\, g(v_\infty;\sigma_v)\xi(m_{\rm pert})\,{\rm d}v_\infty\,{\rm d}m_{\rm pert}, \tag{22}$$

where $n_{\rm tot}$ is the total local stellar density, g is the v_∞ distribution function that integrates to unity over all v_∞ and ξ is the mass function. It is immediately clear by substituting equation 19 into equation 22 that the perturbation rate for hyperbolic encounters is independent of the encounter velocity. The overall differential encounter rate is shown in Figure 1a fixing $\epsilon_{\rm thr} = 0.05$ for illustration. When computing perturbation rates, we hereafter adopt the initial mass function (IMF) similar to that used for the Monte Carlo simulation (see Paper I):

$$\xi(m_*) \propto \begin{cases} m_*^{-\alpha_1} & m_{\rm min} \le m_* < m_{\rm br} \\ m_*^{-\alpha_2} & m_{\rm br} \le m_* \le m_{\rm max} \\ 0 & m_* > m_{\rm max}\ {\rm or}\ m_* < m_{\rm min} \end{cases} \tag{23}$$

for $\alpha_1 = 0.4$, $\alpha_2 = 2.8$, $m_{\rm br} = 0.8\,M_\odot$, $m_{\rm min} = 0.08\,M_\odot$ and $m_{\rm max} = 50\,M_\odot$ and normalisation constants such that ξ is continuous and integrates to unity over all masses. However, we modify the mass function such that ξ is truncated above $m_{\rm max} = 5\,M_\odot$ to exclude short-lived OB stars (main sequence lifetimes shorter than ~ 100 Myr). Note that these stars are still included and evolved for the sake of our Monte Carlo model in Section 3, thus contributing the local velocity dispersion. The asymptotic relative velocity of two stars follows the Maxwell-Boltzmann distribution:

$$g(v_\infty;\sigma_v) = \frac{v_\infty^2}{2\sqrt{\pi}\sigma_v^3}\exp\left(\frac{-v_\infty^2}{4\sigma_v^2}\right) \tag{24}$$

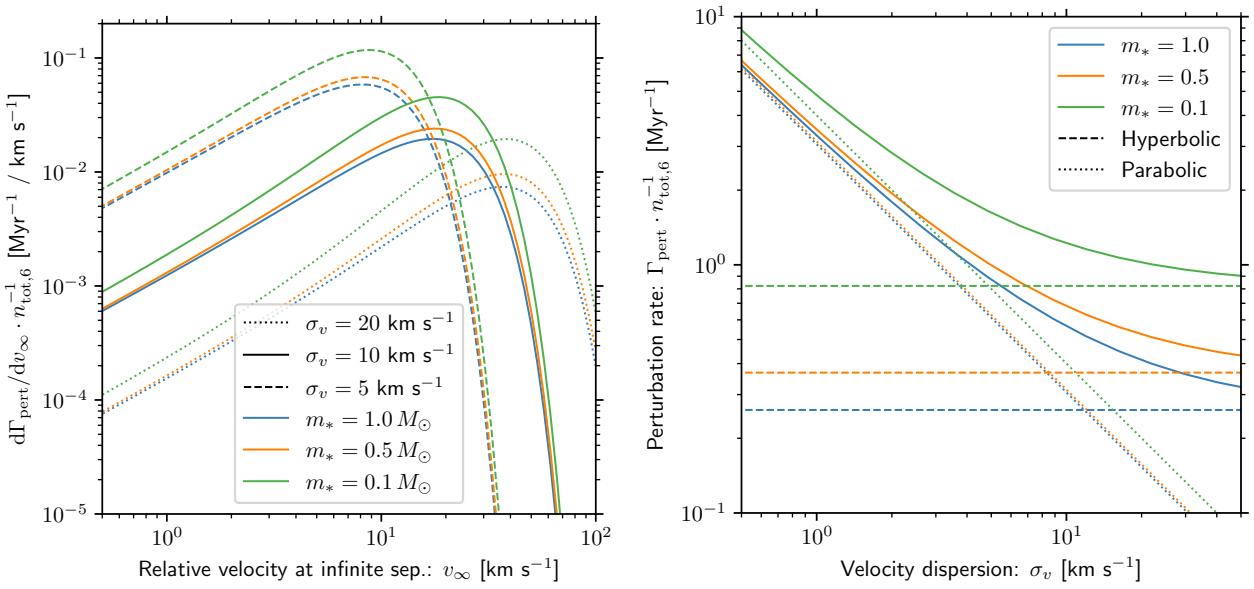

(a) Differential planet perturbation rate with relative speed

(b) Overall planet perturbation rate with velocity dispersion

Figure 1. The rate at which a planet is experiences an encounter that changes the eccentricity by $|\epsilon| > 0.05$. In Figure 1a we show the differential perturbation rate of a planet orbiting with semi-major axis $a_0 = 5$ au and eccentricity $e_0 = 0.9$ in a region of local density $n_{\rm tot}/10^6$ pc$^{-3} = n_{\rm tot,6} = 1$ and varying velocity dispersion σ_v, according to equation 22. In each case, the differential rate is integrated over the perturbers adopting the initial mass function in our Monte Carlo model truncated above 5 $M_\odot$. Integrating these equations over relative velocities gives the overall encounter rates shown in Figure 1b, divided into the hyperbolic (dashed) and parabolic (dotted) components, while the solid line shows the sum of the two.

for three dimensional velocity dispersion σ_v.

The full encounter rate can be obtained by integrating equation 22, as shown in Figure 1b for varying velocity dispersion σ_v. The overall instantaneous perturbation rate can be written:

$$\Gamma_{\rm pert} = \Gamma_{\rm pert}^{\rm (foc)} + \Gamma_{\rm pert}^{\rm (hyp)} \tag{25}$$

where we have split the encounter cross section (and therefore the encounter rate) into a focused and hyperbolic component. The focused component is:

$$\Gamma_{\rm pert}^{\rm (foc)} = 0.052\,(1+q)\epsilon_{\rm thr}^{-2/3} y'^{2/3} \mathcal{M}_*^{\rm (foc)} \frac{n_{\rm tot}}{10^6\,{\rm pc}^{-3}} \frac{a_0}{5\,{\rm au}} \times \times \frac{m_*}{1\,M_\odot} \frac{10\,{\rm km s}^{-1}}{\sigma_v}\,{\rm Myr}^{-1}, \tag{26}$$

with

$$\mathcal{M}_*^{\rm (foc)} = \int_0^\infty {\rm d}m_{\rm pert}\, q_{\rm pert}^{2/3} \left(1+q_{\rm pert}\right)^{2/3} \xi(m_{\rm pert}), \tag{27}$$

for

$$y' = e_0\sqrt{1-e_0^2}. \tag{28}$$

The hyperbolic component is

$$\Gamma_{\rm pert}^{\rm (hyp)} = 0.046\,\sqrt{1+q}\epsilon_{\rm thr}^{-1} y' \mathcal{M}_*^{\rm (hyp)} \frac{n_{\rm tot}}{10^6\,{\rm pc}^{-3}} \times \times \left(\frac{m_*}{1\,M_\odot}\right)^{1/2} \left(\frac{a_0}{5\,{\rm au}}\right)^{3/2} {\rm Myr}^{-1}, \tag{29}$$

with

$$\mathcal{M}_*^{\rm (hyp)} = \int_0^\infty {\rm d}m_{\rm pert}\, q_{\rm pert}\, \xi(m_{\rm pert}) \approx 0.7 \left(\frac{m_*}{1\,M_\odot}\right)^{-1}, \tag{30}$$

where the last approximation is true for our adopted IMF.

The encounter rate described by equation 25 is a shallow function of σ_v and m_* (cf. the tidal capture rate estimates in Paper I). In the limit of large σ_v, $\Gamma_{\rm pert}$ is dominated by the hyperbolic component (equation 29), which is independent of σ_v and only weakly dependent on m_*: $\Gamma_{\rm pert}^{\rm (hyp)} \propto m_*^{-1/2}$. The rate is somewhat dependent on the form of the mass function, but does not exhibit a precipitous decline for low host star masses as in the tidal capture case of Paper I.

2.5 Consequences of the analytic perturbation rates

The expressions for the focused and hyperbolic cross sections (encounter rates) are interesting for two reasons. First, there always exists some small change in eccentricity ϵ such that the growth of eccentricity is dominated by hyperbolic encounters for $\epsilon_{\rm thr} < \epsilon$. Dropping the 'pert' subscript, we consider the perturbation rates $\Gamma^{\rm (foc)}(\epsilon)$ and $\Gamma^{\rm (hyp)}(\epsilon)$ as a function of a small change in eccentricity ϵ. The relative contribution from the two types of encounters at ϵ can be written:

$$\frac{\partial_\epsilon \Gamma^{\rm (hyp)}}{\partial_\epsilon \Gamma^{\rm (foc)}} = \frac{3}{2} C_{\rm hf} y^{1/3} \left[1+q_{\rm pert}\right]^{-1/2} \frac{v_\infty}{v_{\rm orb}} \epsilon^{-1/3}. \tag{31}$$

Setting the LHS of equation 31 equal to one, this gives a condition for the dominance of hyperbolic encounters:

$$\epsilon < \epsilon_{\rm hyp} \equiv \left[\frac{3}{2} C_{\rm hf} \frac{v_\infty}{v_{\rm orb}}\right]^3 \left[1+q_{\rm pert}\right]^{-3/2} y. \tag{32}$$

Given equation 29, we therefore obtain the important result that for a sufficiently large velocity dispersion the distribution of encounters in ϵ space is always the same. The total number of encounters

scales linearly with local density, remaining independent of the local velocity dispersion.

While the condition in equation 32 is strongly dependent on v_∞, for $v_\infty \gtrsim 2v_{\rm orb}$ then $\epsilon_{\rm hyp} \gtrsim 1$ and eccentricity growth is always dominated by hyperbolic encounters (if ionising/resonant encounters are rare). In the context of 47 Tuc and a planet orbiting a solar mass star at semi-major axis $a = 5$ au, we are always in this regime. In Figure 1b, we show that the hyperbolic component dominates for $\sigma_v \gtrsim v_{\rm orb} \approx 10$ km/s for $\epsilon_{\rm thr} = 0.05$. Here, σ_v is the physical three dimensional dispersion. The one dimensional (radial) velocity dispersion towards the centre of 47 Tuc is ~ 12 km s^{-1} (Gebhardt et al. 1995), thus the appropriate σ_v is considerably higher ($\sigma_v \gtrsim 20$ km s^{-1} within 5 pc of the centre – see Paper I). More generally, for sufficiently small ϵ, hyperbolic encounters always dominate. When it comes to how a planet tidally circularises, we are interested in small changes in eccentricity $\epsilon \ll 0.05$. These small changes in eccentricity will turn out to have a strong influence on circularisation. Nonetheless, when $v_{\rm orb}$ exceeds σ_v the hyperbolic encounter rate underestimates the rate of eccentricity change over long time-scales (see Section 2.11.2).

The second interesting consequence of the analytic perturbation rates is that the short-term eccentricity evolution is always dominated by the contribution of weak encounters (small ϵ). As an illustration, we first assume that all encounters positively change the eccentricity. In this case, the rate of change of e due to perturbations is:

$$\dot{e} = \int_{1-e}^{\epsilon} \tilde{\epsilon} \cdot \partial_{\tilde{\epsilon}} \Gamma^{(\rm hyp)} \, {\rm d}\tilde{\epsilon} \propto \ln(1-e) - \ln\epsilon. \tag{33}$$

This diverges as $\epsilon \to 0$, and we thus apparently have infinitely fast eccentricity growth as distant encounters are considered. Notice that this would not be the case if parabolic perturbations dominated. The solution to this apparent paradox is that we have both negative and positive changes to the orbital eccentricity. The evolution of the eccentricities can therefore be modelled as a random-walk (or diffusion) process, which strictly speaking must be treated in the continuum limit. This surprising result will be considered again in terms of our dynamical model in Section 3.3. In Section 2.6 below, we consider the evolution of the probability distribution of the orbital eccentricity as a result of (infinite) distant encounters.

2.6 Statistical eccentricity evolution

2.6.1 *Governing equations*

Given the encounter rate computed in Section 2.4, we can estimate the statistical evolution of the eccentricity of a star-planet system. It is straight forward to show from equations A6 and A9 that in the approximate prescription for the encounter cross section we have applied, the change in eccentricity ϵ due to an encounter has an equal probability of being positive or negative. In Appendix B, we show that if a planet initially has some known eccentricity e_0, then at time $t \lesssim \gamma^{-1}$ the probability density $p(e,t) \equiv {\rm d}N/{\rm d}e$ for N the relative number of planets, follows something similar to the diffusion equation with an extra term:

$$\frac{2}{\gamma}\partial_t p(e,t) \approx \partial_e \left[e\sqrt{1-e^2}\partial_e p(e,t) \right] + \Delta(e,t), \tag{34}$$

where we have defined the diffusion factor

$$\gamma \equiv 0.046\sqrt{1+q}\mathcal{M}_*^{(\rm hyp)} \frac{n_{\rm tot}}{10^6\,{\rm pc}^{-3}} \left(\frac{m_*}{1\,M_\odot}\right)^{1/2} \left(\frac{a_0}{5\,{\rm au}}\right)^{3/2} {\rm Myr}^{-1}, \tag{35}$$

and assumed we are always in the hyperbolic limit for perturbing encounters.

The last term in equation 34 is a non-local term:

$$\Delta \equiv \lim_{\epsilon\to 0}\left\{ \int_{e+\epsilon}^{1} \partial_{\tilde{e}} p(\tilde{e},t) \frac{\tilde{e}\sqrt{1-\tilde{e}^2}}{\tilde{e}-e}\,{\rm d}\tilde{e} - \int_0^{e-\epsilon} \partial_{\tilde{e}} p(\tilde{e},t) \frac{\tilde{e}\sqrt{1-\tilde{e}^2}}{e-\tilde{e}}\,{\rm d}\tilde{e} \right\}. \tag{36}$$

This accounts for the non-zero possibility of large, instantaneous changes in eccentricity due to dynamical encounters, which is in contrast to the usual diffusion scenario, where only local properties of p are important. Although the individual terms on the RHS of equation 36 diverge as $\epsilon \to 0$, we show in Appendix B that the difference between them remains finite such that Δ is well-defined for all e at which $p(e,t)$ is twice continuously differentiable in e. For a given initial distribution $p_0(e) = p(e,0)$, one can therefore solve equation 34 numerically for the time evolution of p.

2.6.2 *Eccentricity evolution and random walk comparison*

The long term evolution of the orbital eccentricity of a planet with an initial eccentricity $e_0 = 0.9$ is shown in Figure 2. We show results for the solution to the initial value problem (IVP) from equation 34 in Figure 2a. We solve the IVP over 1000 grid-points between 0 and 1 in eccentricity space with the fourth order Runge-Kutta method of the `integrate.solve_ivp` module from Scipy (Virtanen et al. 2020). Boundaries are reflective at $e = 0, 1$ and we adopt the initial distribution:

$$p_0(e) = p(e,0) = \frac{1}{\sqrt{2\pi}\sigma_{e,0}} \exp\left(-\frac{(e-e_0)^2}{2\sigma_{e,0}^2} \right) \tag{37}$$

with $\sigma_{e,0} = 10^{-3}$. We see that at early times, the non-local term is negligible and we approximately recover a solution similar to that of the standard diffusion with diffusion coefficient $D \approx \gamma/2 \cdot e\sqrt{1-e^2}$. This solution is just equation 37 with the substitution:

$$\sigma_{e,0}^2 \to 2Dt = \gamma t e\sqrt{1-e^2}. \tag{38}$$

When considering the influence of perturbations on tidal circularisation it will be convenient to apply a stochastic approach, such that individual planet evolution scenarios subject to circularisation tides and external perturbation can be tracked. While it is not possible to model arbitrarily small perturbations from the initial eccentricity, we can perform such an experiment if we are interested in changes of eccentricity greater than some $\epsilon_{\rm min}$.

In order to compare the stochastic eccentricity evolution of a planet to the solution to the IVP, we perform a Monte Carlo experiment wherein we draw a set of random values $u_i \in (0,1)$ where $i = 1, \ldots, N_{\rm res}$. We then compare these with corresponding ξ_i which are the probabilities of a perturbation in time-step of size Δt of size ϵ_i:

$$\xi_i = \gamma e\sqrt{1-e^2}/2 \cdot \Delta t \cdot \Delta\epsilon_i \cdot |\epsilon_i|^{-2}, \tag{39}$$

where $\Delta\epsilon_i$ is the size of the $i^{\rm th}$ eccentricity perturbation bin. For $u_i < \xi_i$, an encounter perturbing the planet by an amount ϵ_i is assumed to have occured within the time-step of size Δt, and is added to the eccentricity for the following time-step. We repeat this for negative and positive ϵ_i – i.e. $\epsilon_i \in (-e, -\epsilon_{\rm min})$ and $\epsilon_i \in (\epsilon_{\rm min}, 1-e)$ respectively. In this instance, the grid in perturbation size ϵ is uniform in ϵ and we adopt $\epsilon_{\rm min} = 10^{-2}$ and $N_{\rm res} = 10^4$.

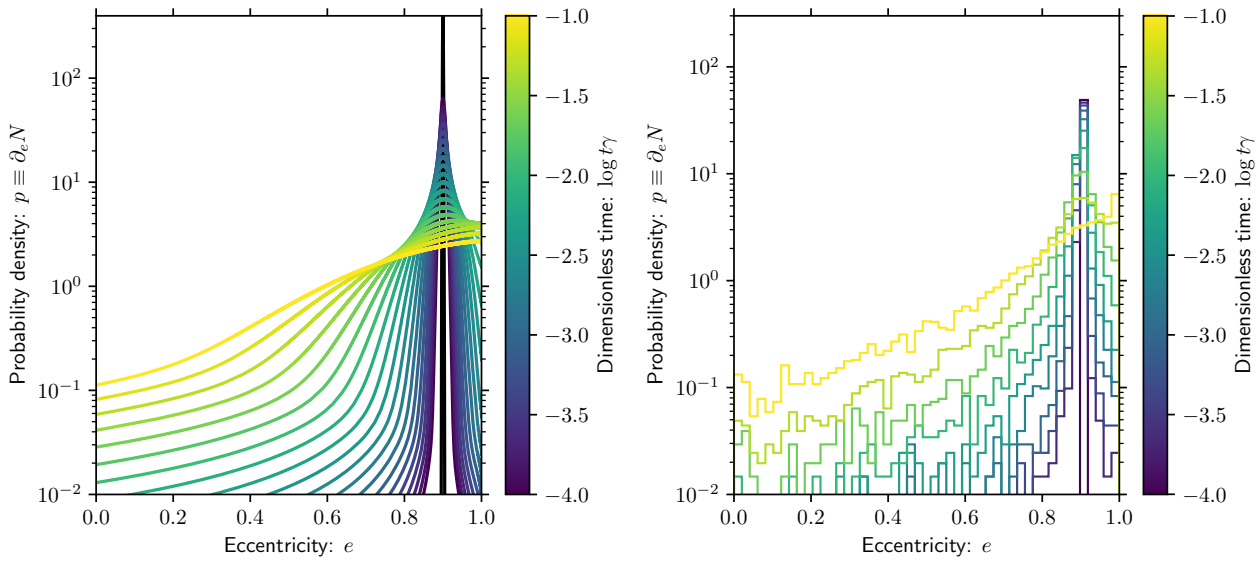

(a) IVP solution

(b) Random walk (10^4)

Figure 2. Evolution of the probability density function $p(e)$ of a planets orbital eccentricity e due to (hyperbolic) dynamical perturbations at fixed semi-major. The time t is normalised by the encounter time-scale γ^{-1} (equation 35), such that the results shown are independent of the absolute encounter rate. Figure 2a shows the result of numerically solving the initial value problem (IVP; equation 34) for an initially Gaussian distribution with mean eccentricity $e_0 = 0.9$ and dispersion $\sigma_{e,0} = 10^{-3}$. Figure 2b is the same but for 10^4 stochastic 'random walk' experiments, where all eccentricities are initially 0.9. Histogram bin sizes are $2 \cdot 10^{-2}$ in eccentricity space. See text for details.

The time-step Δt is chosen such as $\xi_i < 0.1$ everywhere in the grid (i.e. for $\epsilon_{\rm min}$).

The results of 10^4 iterations of this experiment are shown in Figure 2b. For eccentricity bin sizes $2 \cdot 10^{-2}$ (larger than $\epsilon_{\rm min}$) we find good agreement with the direct integration of the IVP in Figure 2a. We conclude that this approach is valid for sufficiently large changes in eccentricity, subject to the choice of $\epsilon_{\rm min}$. This offers an efficient method for computing the evolution of a planet undergoing both perturbations and evolution due to tides, which we will apply again in Section 2.8.1.

2.7 Tidal acceleration

2.7.1 *Maximum circularisation radius*

We are interested in comparing the rate at which eccentricity is changed by external encounters to the rate at which tidal circularisation occurs. Since a planet undergoing purely pseudo-synchronous circularisation conserves the SLR, l, it is useful to consider the change in l over the time $\tau_{\rm circ}$ that a planet takes to circularise as a result of dynamical perturbation. Given our analytic calculation of the eccentricity evolution as a result of hyperbolic encounters (Section 2.6), this change can be approximated:

$$(\Delta l)^2 \approx \int_0^{\tau_{\rm circ}} {\rm d}t\, \gamma e\sqrt{1-e^2} \cdot 4a^2e^2, \tag{40}$$

where the squared term on the LHS comes from the diffusion coefficient in the short term solution to the IVP equation (see equation 38). We can rewrite this in terms of an integral over the semi-major axis a:

$$(\Delta l)^2 \approx \int_{a_0}^{l} {\rm d}a\, \frac{\gamma(a,e)}{\dot a} e\sqrt{1-e^2} \cdot 4a^2e^2, \tag{41}$$

where a_0 is the initial semi-major axis, and eccentricity e is a function of instantaneous semi-major axis a. Again, the SLR l is conserved along the path integral. Now, we have $\dot a = \dot a_{\rm tide}$ and for convenience, we can rewrite equation 11:

$$\dot a = \dot a_{\rm tide} = \alpha_{\rm tide}(e) a^{-7} e^2 (1-e^2)^{-15/2}, \tag{42}$$

where

$$\alpha_{\rm tide} = -21 k_{\rm p} \tau_{\rm p} G m_*^2 M_{\rm p}^{-1} R_{\rm p}^5 f(e^2) \tag{43}$$

is independent of a. Unfortunately, it remains somewhat dependent on eccentricity via the function $f(e^2)$. However, we are primarily interested in large eccentricities, such that for $e \to 1$ we can estimate $f(e^2) \approx 4059/1120$ to simplify the integral. To make the semi-major axis dependence explicit in the integrand of equation 41, we also rewrite:

$$\tilde\gamma \equiv \gamma a^{-3/2}. \tag{44}$$

With this we have

$$(\Delta l)^2 \approx \int_{a_0}^{l} {\rm d}a\, \frac{4\tilde\gamma a^{5/2} l^8}{\alpha_{\rm tide}} = \frac{8\tilde\gamma l^8}{7\alpha_{\rm tide}} \left(a_0^{7/2} - l^{7/2}\right), \tag{45}$$

where in the limit of large initial eccentricity e_0 we also have $a_0 \gg l$.

Finally, our condition for circularisation comes from noting that when the change in eccentricity $\Delta l \to l$, then a planet becomes unlikely to circularise with semi-major axis $\sim l$. Hence, writing $\Delta l/l < 1$, we have an expression for the maximum allowed SLR:

$$l_{\rm max} = C_\Delta \left(\frac{7\alpha_{\rm tide}}{8\tilde\gamma a_0^{7/2}}\right)^{1/6}, \tag{46}$$

or more helpfully:

$$\left(\frac{l_{\rm max}}{0.02\,{\rm au}}\right)^6 = 1.9\,C_\Delta\,\frac{k_{\rm p}}{0.25}\frac{\tau_{\rm p}}{0.66\,{\rm s}}\left(\frac{m_*}{1\,M_\odot}\right)^2\left(\frac{M_{\rm p}}{1\,M_{\rm J}}\right)^{-1}\times \\ \times\left(\frac{R_{\rm p}}{0.1\,R_\odot}\right)^5\left(\frac{a_0}{5\,{\rm au}}\right)^{-2}\left(\frac{\gamma_0}{10^{-4}\,{\rm Myr}^{-1}}\right)^{-1}, \quad (47)$$

where $\gamma_0 = \gamma(a_0)$. We have introduced a correction term C_Δ that originates from the modification of the encounter rate γ_0 to incorporate the non-local term in the PDE that governs the probability density function for e (i.e. Δ in equation 34). This term becomes important for the largest values of the minimum eccentricity required to circularise:

$$e_{\rm min} = \sqrt{1 - \frac{l_{\rm max}}{a_0}}. \quad (48)$$

As $e_{\rm min} \to 1$, the diffusive term in equation 34 at $l_{\rm max}$ becomes small. In this case, encounters that produce $l \lesssim l_{\rm max}$ may become dominated by the non-local term. Because $l_{\rm max}$ scales only with $C_\Delta^{1/6}$ this correction factor only has a moderate (order unity) influence on $l_{\rm max}$ across any reasonable range of γ_0. We will initially adopt $C_\Delta = 1$, and revisit this value in Section 2.8 and Appendix C.

Substituting in $\gamma_0 = \gamma$ from equation 35 yields a version of equation 47 that is similar (although not identical) to the estimate of the final semi-major axis given by equation 37 of HT17, which is derived in a different way. The expression highlights that the maximum angular momentum (or SLR) at which a planet can circularise is very weakly dependent on the encounter rate parameter γ. This is because the rate of tidal circularisation is very strongly dependent on l. Nonetheless, the typical l for HJs coincides with a sensible density range for dense stellar clusters. HJs have $l \sim 0.02$–0.1 au, with only a factor of a few in dynamical range; the shortest period HJ discovered has a semi-major axis of 0.0143 au (McCormac et al. 2020). For sensible encounter rates, $10^{-7}\,{\rm Myr}^{-1} \lesssim \gamma \lesssim 10^{-1}\,{\rm Myr}^{-1}$ ($1\,{\rm pc}^{-3} \lesssim {\rm n_{tot}} \lesssim 10^6\,{\rm pc}^{-3}$), we are in the interesting regime, for which the typical HJ $l \sim l_{\rm max}$, given reasonable initial orbital, stellar and planetary properties. In general, density can vary by several orders of magnitude even within the same cluster environment, which may therefore result in a change of a factor several in the typical circularisation radii l.

2.7.2 *Critical stellar density*

We can recast equation 47 into a critical number density, comparable to that inferred by HT17. From equation 35 we have $\gamma \propto n_{\rm tot}$, the local density. By assuming that HJ formation requires $l_{\rm max} \gtrsim 0.02$ au, we can rewrite equation 47 to yield:

$$n_{\rm crit} \sim 5\cdot 10^3\,{\rm pc}^{-3}\,\frac{1}{\mathcal{M}_*^{\rm (hyp)}}\frac{\rm k_p}{0.25}\frac{\tau_{\rm p}}{0.66\,{\rm s}}\left(\frac{\rm m_*}{1\,{\rm M}_\odot}\right)^{3/2}\left(\frac{\rm M_p}{1\,{\rm M_J}}\right)^{-1}\times \\ \times\left(\frac{R_{\rm p}}{0.1\,R_\odot}\right)^5\left(\frac{a_0}{5\,{\rm au}}\right)^{-7/2}, \quad (49)$$

where we have assumed $q \ll 1$. This density is comparable to that inferred by HT17, see their equation 40. Unlike the expression in that work, our expression is not dependent on the local velocity dispersion or encounter radius because we have used the general expression for eccentricity evolution as a function of many distant, hyperbolic encounters. This has similarly allowed us to eliminate the initial pericentre distance, or equivalently eccentricity, as a free parameter. However, while the scaling in equation 49 is accurate, the normalisation is somewhat arbitrary due to the strong dependence on the choice of $l_{\rm max}$ threshold (equivalently, the initial pericentre distance in the derivation by HT17). We will therefore consider a more useful metric, which is the destruction fraction itself; we quantify this fraction by first considering the distribution of circularisation radii due to encounters (Section 2.8) and then the conditions for HJ survival (Section 2.9).

2.7.3 *Circularisation time-scale and the low density limit*

One can also interpret the threshold we have derived by considering the rate of acceleration of tidal circularisation. The change in l from equation 41 is dominated by encounters for maximal a – i.e. $a = a_0$. We therefore obtain a similar requirement for l by considering the initial, instantaneous rate of change of the tidal circularisation time-scale:

$$\tau_{\rm circ} = \left(\frac{\dot{a}_{\rm tide}^2}{a^2} + \dot{e}_{\rm tide}^2\right)^{-1/2} \quad (50)$$

when $a \gg l$ and large e. If

$$\dot{\tau}_{\rm circ} = \frac{\gamma}{2}e\sqrt{1-e^2}\,\partial_e\tau_{\rm circ} \lesssim 1, \quad (51)$$

then the rate of change of the circularisation rate is slower than the rate of circularisation itself. This means that over the time required for a planet to circularise, $\tau_{\rm circ}$ (or equivalently the SLR, l) remains approximately constant. Computing equation 51 yields a condition for l similar to expression 47. With this interpretation, it is understood that HJ circularisation radii are limited by the initial rate of tidal acceleration relative to circularisation time-scale in a sufficiently dense cluster environment.

With the definition of the circularisation time-scale, there exists a further constraint on the possible values of the SLR l for circularisation to occur. In the limit of low e (or large a), the time-scale for circularisation $\tau_{\rm circ}$ will exceed the age of the system. From equations 11, 12 and 50, we have:

$$\frac{\tau_{\rm age}}{\tau_{\rm circ}} = \tau_{\rm age}\cdot|\alpha_{\rm tide}|\frac{e}{a^8(1-e^2)^{13/2}}\sqrt{\frac{1}{4}+\frac{e^2}{(1-e^2)^2}}. \quad (52)$$

By requiring that the LHS of equation 52 is greater than one, we have the requirement for circularisation:

$$l < l_{\rm age}, \quad (53)$$

where

$$\left(\frac{l_{\rm age}}{0.02\,{\rm au}}\right)^{15/2} = 2400\frac{\tau_{\rm age}}{10\,{\rm Gyr}}\cdot f(e^2)\frac{k_{\rm p}}{0.25}\frac{\tau_{\rm p}}{0.66\,{\rm s}}\left(\frac{m_*}{1\,M_\odot}\right)^2\times \\ \times\left(\frac{M_{\rm p}}{1\,M_{\rm J}}\right)^{-1}\left(\frac{R_{\rm p}}{0.1\,R_\odot}\right)^5\left(\frac{a}{5\,{\rm au}}\right)^{-1/2}e\sqrt{\frac{(1-e^2)^2}{4}+e^2}, \quad (54)$$

and we have substituted $\alpha_{\rm tide}$ from equation 43:

$$\alpha_{\rm tide}\cdot(0.02\,{\rm au})^{-15/2}\cdot(5\,{\rm au})^{-1/2} = -240\cdot f(e^2)\frac{k_{\rm p}}{0.25}\frac{\tau_{\rm p}}{0.66\,{\rm s}}\times \\ \times\left(\frac{m_*}{1\,M_\odot}\right)^2\left(\frac{M_{\rm p}}{1\,M_{\rm J}}\right)^{-1}\left(\frac{R_{\rm p}}{0.1\,R_\odot}\right)^5\,{\rm Gyr}^{-1}. \quad (55)$$

Equation 54 is simplified by adopting $e \approx 1$ and thus $f = 4059/1120$ as before. In this way, we obtain the second maximal constraint $l_{\rm age}$ as a function of semi-major axis a.

2.8 Circularisation radii

2.8.1 *Random walk with circularisation*

In order for a planet to migrate via HEM, it must reach a sufficiently high eccentricity such that tidal forces act more quickly to shrink the orbit than external perturbations act to alter the eccentricity. This is achieved at $l_{\rm max}$, the SLR that yields a balance between tidal forces and perturbative encounter rates. If such an eccentricity is reached due to external perturbations, we have shown that the short term eccentricity evolution is a diffusive process. Thus we expect the SLR l of the planet to fluctuate close to $l_{\rm max}$ before finally circularising. Thus, if the SLR is conserved under tidal circularisation, the typical circularisation radii for HJs approximately coincide with $l_{\rm max}$.

We therefore proceed on the assumption that encounters play an important role in determining the circularisation radii of HJs. If initially very extreme eccentricities that yield orbits that can circularise ($l > l_{\rm max}$) are rare, then the distribution of circularisation radii l achieved by the diffusive eccentricity evolution should only depend on the value of $l_{\rm max}$ (we use the SLR l interchangeably with circularisation radius, since $a = l$ for $e = 0$). Working on this principle, we perform the following numerical experiment to quantify the distribution of circularisation radii.

We perform a similar random walk calculation as described in Section 2.6.2, but this time include tidal circularisation. In order to ensure that all potentially important encounters are included, we this time adopt a minimum change in eccentricity $\epsilon_{\rm min} = 5 \cdot 10^{-6}$ from a single encounter. Here we define our grid of 10^4 ϵ values to be logarithmic spaced in $1-e$ between $\epsilon_{\rm min}$ and $1-\epsilon_{\rm min}$, such that changes that yield large eccentricities – i.e. those in which we are primarily interested – are well-resolved. Circularisation is treated with a $4^{\rm th}$ order Runge-Kutta scheme, following equations 11 and 12, while the time-step is determined by the most stringent of several conditions. The first is simply the Courant–Friedrichs–Lewy condition for the rate of circularisation. Secondly, to ensure that the fractional change of semi-major axis is small so as to allow accurate computation of the encounter rate in a given time-step, we also ensure that the semi-major axis $|\Delta a| < a/10$. Finally, we must avoid rapid changes to the circularisation radius (rate) due to encounters within successive time-steps. We achieve this by ensuring that encounters that give large change in the eccentricity $\Delta e_{\rm pert}$ due to all perturbations on a given time-step do not frequently (on successive time-steps) exceed certain values. Perturbations that give $\Delta e_{\rm pert} > 1 - e_{\rm min}$ are considered too large. In addition, we ensure a dimensionless acceleration parameter remains small:

$$C = C_a + C_e < C_{\rm max} \tag{56}$$

where

$$C_a = \Delta t \left| \frac{\dot{a}_{\rm tide}(a, e + \Delta e_{\rm pert}) - \dot{a}_{\rm tide}(e)}{\dot{a}_{\rm tide}(a, e)} \cdot \frac{\dot{a}_{\rm tide}(a, e + \Delta e_{\rm pert})}{a} \right|, \tag{57}$$

and similar for C_e but substituting $e, \dot{e}_{\rm tide}$ instead of $a, \dot{a}_{\rm tide}$. The value of C is large if the acceleration of the circularisation rate and the resultant change of semi-major axis per time-step are large. By ensuring Δt remains small enough to keep C small, we ensure that we do not allow the planet to 'walk' into and out of a region in a–e space in which it should go through rapid circularisation within a single time-step. We must still allow for occasional large instantaneous changes in eccentricity, thus these conditions may be violated on a single time-step. However, such events should be infrequent – i.e. not occurring on successive time-steps. We reduce Δt by an order of magnitude if $C > C_{\rm max} = 0.1$ or $\Delta e_{\rm pert} > 1 - e_{\rm min}$. Testing with different thresholds yields similar results.

For initial conditions, we draw semi-major axis from a log-normal distribution with a mean at $\log(a/1\,{\rm au}) = 0.5$ with 0.5 dex scatter, and fix the initial eccentricity $e_0 = 0.1$. We choose this to better reflect a sensible initial eccentricity of a planet (e.g. Dunhill et al. 2013), rather than one that has already been excited to high eccentricity by dynamical interactions. We evolve each realisation for 12 Gyr. The results of this experiment are shown in Figure 3 for three different values of $\gamma(a)$ at $a = 5$ au. The red line in each plot traces the value of $l_{\rm max}$ in a–e space, assuming $C_\Delta = 1$ and adopting $a_0 = a$. As γ increases, $l_{\rm max}$ decreases. In each case, $l_{\rm max}$ traces the maximal possible circularisation radius. This suggests that the tidal acceleration condition discussed in Section 2.7 is appropriate.

One counter-intuitive consequence of the tidal acceleration condition is that it becomes difficult to circularise planets on wide orbits, despite higher perturbation rates. This is because $l_{\rm max}$ decreases with increasing a. For systems that start at large a, or occupy dense regions and are therefore subject to more frequent perturbations, tidal inspiral only dominates over perturbations for values of l that are so low that it becomes hard to avoid tidal destruction of the planet (see Section 2.9). Thus HEM migration may be efficiently suppressed at sufficiently high densities.

2.8.2 *Analytic circularisation radius distribution*

We are interested in how tidal acceleration influences the fraction of planets that do not survive circularisation. In order to do this, we must first relate the maximum value to the overall distribution of circularisation radii (or l values). To this end, we first define the normalised SLR:

$$l' \equiv l_{\rm min}/l_{\rm max}. \tag{58}$$

In this expression we have introduced $l_{\rm min}$, which is the lowest value of l reached by a circularising planet. This value is of interest because if the majority of dynamical perturbations occur early during circularisation, then this quantity relates directly to the smallest pericentre distance reached. As discussed in Section 2.9, this distance determines whether the would-be HJ survives. In defining $l_{\rm max}$, we here adopt equation 47 with the correction factor C_Δ estimated as in Appendix C.

We now search for sensible probability density function $p(l')$ that describes the distribution of l' at any given perturbation rate γ. In the absence of greater constraints, the functional form should have support in the range $(0, \infty)$ and yield $p(l')$ that drops to zero as l' exceeds unity. We choose an exponential distribution, which is a maximal entropy solution that satisfies this condition:

$$p(l') = \exp(-l'). \tag{59}$$

We compare the probability distribution given by our heuristic equation 59 to the distribution of l' for circularised planets obtained from the numerical random walk experiment described in Section 2.8.1. We find that the median of the analytic distribution is always within one standard deviation of the random walk medians, and by eye we have reasonable agreement between the overall shape across two orders of magnitude in the encounter rate (we exclude $\gamma(5\,{\rm au}) = 10^{-4}$ due to the low number of circularised planets in our simulations). Given that we have achieved reasonable agreement with a simple and maximal entropy distribution without any degrees of freedom, we do not perform a formal statistical comparison with alternative models and fitting parameters. We hence adopt equation 59 to simplify computation of the survival rates of HJs as follows.

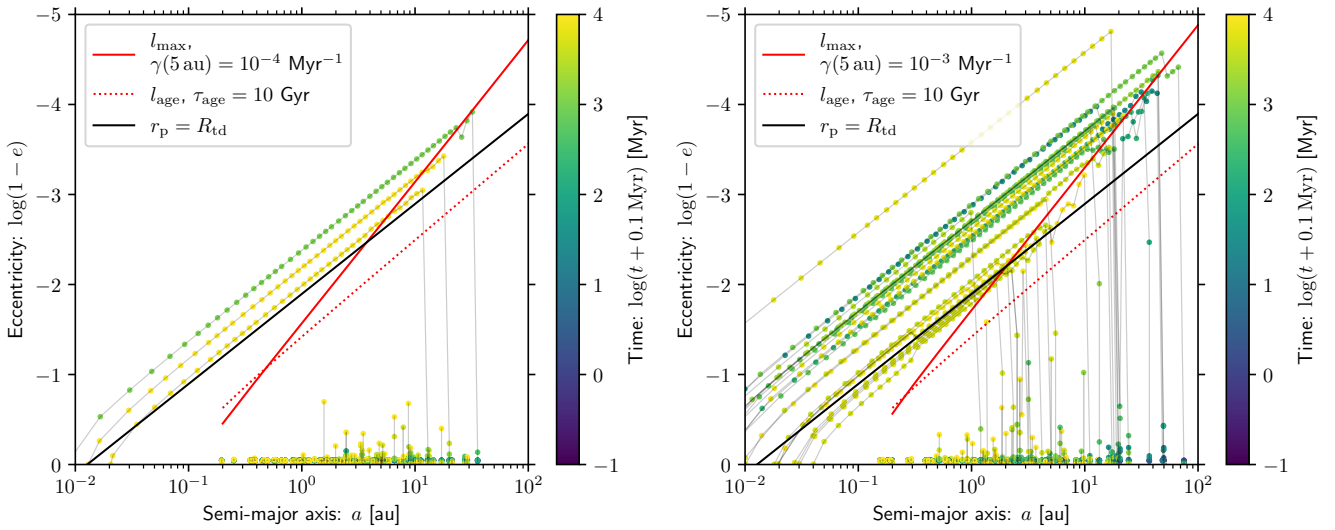

(a) $\gamma = 10^{-4}$ Myr^{-1} at $a = 5$ au

(b) $\gamma = 10^{-3}$ Myr^{-1} at $a = 5$ au

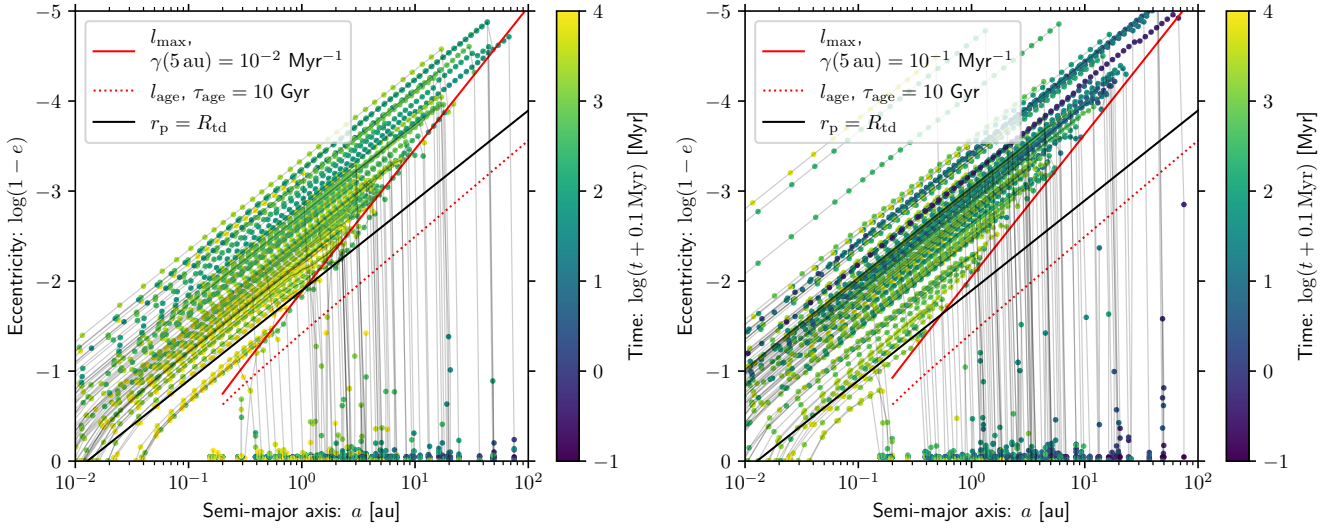

(c) $\gamma = 10^{-2}$ Myr^{-1} at $a = 5$ au

(d) $\gamma = 10^{-1}$ Myr^{-1} at $a = 5$ au

Figure 3. The eccentricity e and semi-major axis a evolution resulting from one hundred numerical experiments for the stochastic perturbations to the orbital eccentricity with tidal circularisation. Planets are initialised with a log-normal semi-major axis (mean $\overline{\log a/1\,\mathrm{au}} = 0.5$, 0.5 dex dispersion) and initial eccentricity $e_0 = 0.1$. They evolve due to perturbations, undergoing a random walk in the y-axis (eccentricity space). The planets are always subject to tidal forces from the host star, which try to circularise the planet while conserving SLR, $l = a(1-e^2)$. However, tides can only circularise the planet efficiently when $l < l_{\max}$, which we estimate analytically using equation 47, here with $C_\Delta = 1$, shown as a solid red line. The numerical experiment shows good agreement with the analytic expression. The dotted red line shows the maximum SLR, l_{age}, for which a planet can circularise over the age of the system ($\tau_{\mathrm{age}} = 10$ Gyr), using equation 54. Each panel shows a different value of the local encounter rate, parameterised by γ at 5 au. The time intervals are shown as coloured points by the time indicated in the colour bar, with faint connecting lines for each realisation. The black line shows the tidal destruction radius R_{td}, discussed in Section 2.9. Thus, most of the circularised HJs for these experiments would physically be tidally destroyed rather than circularise; circularisation requires slower encounter rates. However, we continue to evolve planets when pericentre distances $r_{\mathrm{p}} < R_{\mathrm{td}}$ because here we are only interested in the final circularisation radii due to the tidal forces and external eccentricity perturbations.

2.9 Hot Jupiter survival

For sufficiently small pericentre distance r_{p} (or l), a would-be HJ may not survive the circularisation process. Of course, we immediately have $r_{\mathrm{p}} > R_* + R_{\mathrm{p}}$ to avoid collision. However, more stringently Guillochon et al. (2011) estimate that to avoid destruction or ejection (due to asymmetric mass removal) they must have radius greater than:

$$r_{\mathrm{p}} > R_{\mathrm{td}} = \eta R_{\mathrm{Roche}} = 6.8 \times 10^{-3} \cdot \eta \cdot \frac{R_{\mathrm{p}}}{0.1\,\mathrm{au}} \left(\frac{m_*}{1\,M_\odot}\right)^{1/3} \left(\frac{M_{\mathrm{p}}}{1\,M_{\mathrm{J}}}\right)^{-1/3} \mathrm{au}, \quad (60)$$

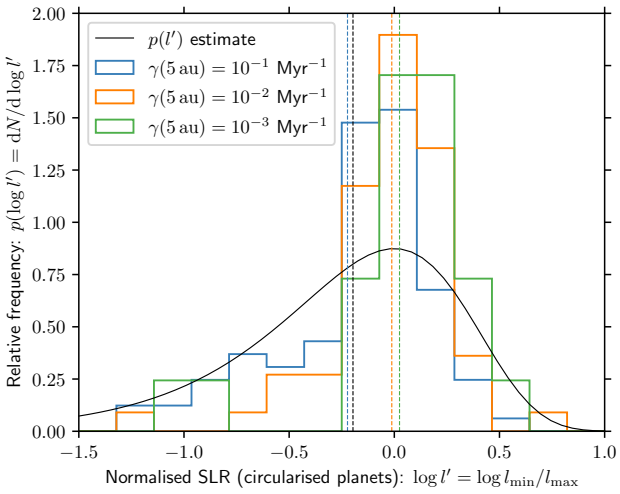

Figure 4. Histogram of the minimum semi-latus rectum (SLR, $l_{\rm min}$) distribution for the planets that eventually circularise (defined to have final $e < 10^{-3}$, and $a < 0.1$ au) in the suite of random walk simulations. The minimum SLR is normalised by the maximum value $l_{\rm max}$ predicted theoretically using equation 47. Our heuristic estimate for the distribution of $l' = l_{\rm min}/l_{\rm max}$, as described by equation 59, is shown as a black line. The logarithmic mean of each distribution is shown as a vertical in the appropriate colour.

where $R_{\rm Roche}$ is the Roche radius and $\eta \approx 1.87$ to give $R_{\rm td} \approx 0.013$ au for a solar mass star and a Jupiter-like planet. We show this tidal destruction contour in a–e space as a black line in Figure 3. However, at this stage we have allowed the planet orbits to evolve in the absence of tidal destruction, since we are interested in the final distribution of circulisation radii due to tidal forces and external eccentricity perturbations.

We now wish to relate the survival condition to the distribution of circularisation radii. The pericentre of the circularising planet is related to the maximum SLR $l_{\rm max}$ of a planet with initial eccentricity e_0, semi-major axis a_0 by the expression:

$$r_{\rm p,max} = l_{\rm max}/(1+e_0) = \frac{l_{\rm max}}{1+\sqrt{1-l_{\rm max}/a_0}}. \tag{61}$$

For large $a_0 \gg l_{\rm max}$ (requiring large e_0 for circularisation), we have $r_{\rm p,max} \approx l_{\rm max}/2$. We then define:

$$x \equiv \frac{r_{\rm p}}{R_{\rm td}} \approx \frac{l}{2R_{\rm td}}. \tag{62}$$

We can write the maximum value of this ratio:

$$x_{\rm max} = \frac{r_{\rm p,max}}{R_{\rm td}} \approx \frac{3.67}{\eta}\frac{l_{\rm max}}{0.05\,\mathrm{au}}\left(\frac{R_{\rm p}}{0.1\,\mathrm{au}}\right)^{-1}\left(\frac{m_*}{1\,M_\odot}\right)^{-1/3}\left(\frac{M_{\rm p}}{1\,M_{\rm J}}\right)^{1/3}, \tag{63}$$

where $l_{\rm max}$ is evaluated via equation 47 and the prefactor $3.67/\eta \approx 2$. Since $x \propto l$ and $x_{\rm max} \propto l_{\rm max}$, we can also define $x' = x/x_{\rm max}$ to give $p(x') \propto p(l')$. Now the fraction of circularising planets that are tidally destroyed is:

$$f_{\rm td} = \int_0^{\frac{1}{x_{\rm max}}} p(x')\mathrm{d}x' = 1 - \exp(-1/x_{\rm max}), \tag{64}$$

where the integral is evaluated using the form of $p(x')$ from equation 59.

2.10 Ionisation rate

In the close encounter limit, the orbital energy as well as angular momentum is changed, which can lead to ionisation or exchange of the planet. The corresponding scattering cross-section $\sigma_{\rm ion}$ for equal mass components following Hut & Bahcall (1983) is:

$$\sigma_{\rm ion} \approx \frac{20}{9}\pi q_{\rm pert}^{1/3} a_0^2 \left(\frac{v_{\rm c}}{v_\infty}\right)^2, \tag{65}$$

where $q_{\rm pert} = m_{\rm pert}/m_*$ and

$$v_{\rm c}^2 = \frac{G m_{\rm tot}}{a_0}, \tag{66}$$

for total mass $m_{\rm tot}$. Fregeau et al. (2004) find that the scattering cross-section is almost independent of the binary mass-ratio q. Finally, the scaling with $q_{\rm pert}^{1/3}$ is an approximation based on the scaling in the test particle limit for a gravitationally focused encounter (Ostriker 1994; Breslau et al. 2014; Winter et al. 2018a).

The cross section from equation 65 can be converted to an encounter rate in the same way as in Section 2.4 for the perturbation rate. That is:

$$\mathrm{d}\Gamma_{\rm ion} = v_\infty n_{\rm tot}\sigma_{\rm ion} g(v_\infty;\sigma_v)\xi(m_{\rm pert})\,\mathrm{d}v_\infty \mathrm{d}m_{\rm pert} \tag{67}$$

to give:

$$\Gamma_{\rm ion} = 0.028\mathcal{M}_*^{\rm (ion)}\left(\frac{\sigma_v}{10\,\mathrm{km\,s^{-1}}}\right)^{-1}\frac{m_*}{1\,M_\odot}\times \times\frac{a_0}{5\,\mathrm{au}}\frac{n_{\rm tot}}{10^6\,\mathrm{pc^{-3}}}\,\mathrm{Myr}^{-1}. \tag{68}$$

Here we have defined:

$$\mathcal{M}_*^{\rm (ion)} = \int_0^\infty \mathrm{d}m_{\rm pert}\,(1+q_{\rm pert}+q)q_{\rm pert}^{1/3}\xi(m_{\rm pert}). \tag{69}$$

Comparing to equation 29, we see that the ionisation rate is comparable to the rate at which extreme eccentricities are excited in a single encounter ($\epsilon_{\rm thr} \sim 1$). We also see that the dominant type of encounter depends on the local velocity dispersion σ_v.

2.11 Fractional outcomes

2.11.1 Analytic expressions

We now consider the fraction of planets that are ionised compared to those that are circularised or tidally destroyed in an environment with fixed properties ($n_{\rm tot}, \sigma_v$). We first simply make the distinction between ionised planets and those influenced by tides, regardless of whether a planet is circularised or destroyed. The relevant probabilities satisfy:

$$P_{\rm tide} + P_{\rm ion} = 1 - \exp\left[-(\Gamma_{\rm ion}+\Gamma_{\rm tide})t\right], \tag{70}$$

where $P_{\rm tide}$, $P_{\rm ion}$ is the cumulative probability of a planet being tidally influenced or ionised respectively. We have also used the tidal rate:

$$\Gamma_{\rm tide} \approx \frac{\gamma_0 e_0\sqrt{1-e_0}}{2(e_{\rm tide}-e_0)} \tag{71}$$

for

$$e_{\rm tide} = \min\left\{\max\{e_{\rm min}, e_{\rm age}\}, e_{\rm td}\right\} \tag{72}$$

where

$$e_{\rm min} = \sqrt{1-\frac{l_{\rm max}}{a_0}} \tag{73}$$

is the minimum eccentricity required for tidal forces to dominate over perturbative encounters and

$$e_{\rm age} = \sqrt{1 - \frac{l_{\rm age}}{a_0}} \tag{74}$$

is the minimum eccentricity that allows circularisation over the age of the system. Finally

$$e_{\rm td} = 1 - \frac{R_{\rm td}}{a_0} \tag{75}$$

is the eccentricity above which the planet will be tidally disrupted at periastron. Equation 71 is the rate at which individual encounters perturb a planet with initial eccentricity e_0 to eccentricity $> e_{\rm tide}$. This estimate is justified in Appendix C, in which we compare with the circularisation times obtained from our random walk experiments.

With these rates, we can write the differential equations that govern each probability:

$$\dot{P}_{\rm tide} = (1 - P_{\rm tide} - P_{\rm ion})\Gamma_{\rm tide} \tag{76}$$

$$\dot{P}_{\rm ion} = (1 - P_{\rm tide} - P_{\rm ion})\Gamma_{\rm ion}. \tag{77}$$

The solutions to these equations are simply:

$$P_{\rm tide} = \frac{\Gamma_{\rm tide}}{\Gamma_{\rm tide} + \Gamma_{\rm ion}} \{1 - \exp\left[-(\Gamma_{\rm ion} + \Gamma_{\rm tide})t\right]\} \tag{78}$$

$$P_{\rm ion} = \frac{\Gamma_{\rm ion}}{\Gamma_{\rm tide} + \Gamma_{\rm ion}} \{1 - \exp\left[-(\Gamma_{\rm ion} + \Gamma_{\rm tide})t\right]\}. \tag{79}$$

Finally, we have:

$$P_{\rm HJ} = (1 - f_{\rm td})P_{\rm tide} \qquad P_{\rm td} = f_{\rm td}P_{\rm tide}, \tag{80}$$

where $P_{\rm HJ}$, $P_{\rm td}$ are the probabilities of HJ formation or tidal destruction respectively, and $f_{\rm td}$ is defined by equation 64. Equations 78, 79 and 80 are an analytic approximation for the relative fractions of the three outcomes as a function of time in any dense stellar environment.

2.11.2 *Comparison to simulation results*

HT17 performed simulations tracking the evolution of massive planets under the influence of external perturbations and stellar tides for 10 Gyr at constant local stellar density $n_{\rm tot}$ and velocity dispersion σ_v, including only encounters within a certain radius $R_{\rm enc}$. We here compare our analytic estimates to the outcomes of those experiements, particularly in Figure 5 of that work. The authors use a mass function that is initially that of Salpeter (1955), but evolved for 5 Gyr. We approximately reproduce this mass function by truncating the mass function above $m_{\rm pert} = 1.3\,M_\odot$. We adopt the same $\sigma_v = 6$ km s^{-1} and $m_* = 1\,M_\odot$. The authors also adopt a Rayleigh distribution in e_0, with a rms of 0.33 and truncated above $e_0 = 0.6$. We adopt $e_0 = 0.3$ as a typical initial eccentricity.

The results of our analytic calculations are shown in Figure 5 for initial semi-major axes $a_0 = 1$ au and $a_0 = 4$ au. We compare the results of the simulations performed by experiment for the $a_0 = 1$ au case with $R_{\rm enc} = 100$ au, as tabulated by HT17. The $a_0 = 4$ au outcomes are not tabulated in that study, but can be visually compared with Figure 5 in that work.

For the $a_0 = 1$ au case, we find that our analytic expressions qualitatively reproduce the numerical experiment outcomes. HJ production peaks around $n_{\rm crit} \sim 3 \cdot 10^4$ pc^{-3}, while the tidal destruction fraction continues to increase slowly with density. The

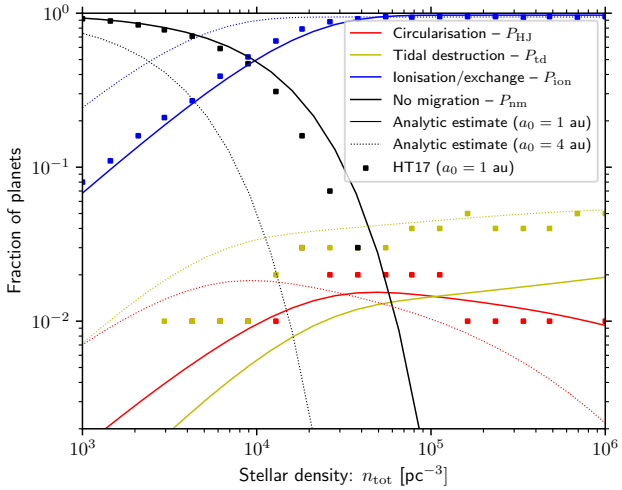

Figure 5. Direct comparison between the outcome probabilities for planets in a dense environment computed with the analytic approximation presented in this work (solid lines) versus those obtained by the numerical experiments of HT17, square points. The results for are shown for initial semi-major axis $a_0 = 1$ au and $e_0 = 0.3$, stellar mass $m_* = 1\,M_\odot$, velocity dispersion $\sigma_v = 6$ km s^{-1}, planetary radius $R_{\rm p} = 1\,R_{\rm J}$ and mass $M_{\rm p} = 1\,M_{\rm J}$. The dotted lines are the theoretical results but for $a_0 = 4$ au, which show good agreement with the simulation results shown in Figure 5 of HT17. For the simulations, the authors adopt an encounter radius $R_{\rm enc} = 100$ au. Results are computed over a time interval of 10 Gyr at each stellar density $n_{\rm tot}$, while the assumed mass function of perturbers is fixed to be appropriate at 5 Gyr. Ionisation and transfer outcomes are shown as blue lines, red lines show planets that undergo circularisation (hot or warm Jupiters), yellow-green lines are for tidal destruction, while black lines are for the planets that undergo no significant migration. See text for details.

only quantitative disagreement is that the analytic results underpredict the frequency of tidal destruction outcomes by a factor ~ 2. This may be due to the regime of the experiments performed by HT17. In particular, the $a_0 = 1$ au case has large $v_{\rm orb} \gg \sigma_v$ in this case. Our treatment addresses encounters with $v_{\rm orb} \lesssim \sigma_v$, and we ignore parabolic encounters such that we may underestimate the number of perturbations that result in large eccentricity changes (see Section 2.5). Comparison with the $a_0 = 4$ au results (with smaller $v_{\rm orb}$) again demonstrate good qualitative agreement with all the outcomes. Quantitatively, we slightly overestimate the tidal outcomes (destruction and circularisation) by a factor of order unity. This may be due to an overestimate of $\Gamma_{\rm tide}$ (see Appendix C), or the fact that we adopt a single initial eccentricity $e_0 = 0.3$ rather than the distribution of HT17. Nonetheless, our results remain a good estimate and within the Poisson error (0.02 for the 2000 realisations) of the Monte Carlo experiments of HT17. We conclude that our analytic estimate is appropriate for sufficiently large σ_v and/or a_0.

2.12 Summary

In Section 2 we have reduced the question of the statistical evolution of planetary systems in dense environments to an evaluation of the local conditions during their evolution. We therefore need only track these conditions within a given dynamical model to obtain fractional expected outcomes. We apply these results to a dynamical model for 47 Tuc in Section 3.

3 APPLICATION TO 47 TUC

3.1 Summary of Section 2

In Section 2 we developed an analytic framework for computing the statistical likelihood of four possible outcomes for a planet orbiting a star in a dense stellar environment. The possible outcomes are:

(i) *No migration:* The orbital energy of the planet is not greatly altered from the initial energy.
(ii) *Circularisation:* The orbital eccentricity is sufficiently excited by stellar encounters to yield a periastron distance of a few stellar radii. In this case, the planet feels strong tidal forces at periastron that allow it to migrate to a short-period orbit over its lifetime.
(iii) *Tidal disruption:* The rate of dynamical perturbation is so rapid that the planet cannot circularise in the usual way without already having undergoing further changes to its eccentricity. As the encounter rate increases, the periastron distance required for circularisation to act more quickly than dynamical perturbations decreases. For sufficiently fast encounter rates, the planet becomes tidally disrupted at closest approach with the host star.
(iv) *Ionisation/exchange:* The star-planet system is disrupted due to a close encounter that imparts kinetic energy and unbinds the planet.

Having analytically quantified the relative frequencies of each of these outcomes, given system and environmental properties, we benchmarked our results against numerical experiments. Given the agreement between the analytic expectation and the simulation results, we here apply our analytic framework to a dynamical model of 47 Tuc. For this globular cluster there exist observational constraints on the fraction of HJs.

3.2 Summary of observational constraints

In this section we consider the expected efficiency of HJ production with respect to the observational constraints. In terms of the latter, the transit survey by GBG+00 is discussed in some detail in Paper I. In brief, 34,091 stars were observed with visual magnitudes in the range $17.1 < V < 21.1$, bounded by sensitivity constraints and the requirement that all target stars remain on the main sequence. This corresponds to stellar masses $0.52\,M_\odot < m_* < 0.88\,M_\odot$ (Bergbusch & Vandenberg 1992) and the targets were typically separated from the cluster centre by a (projected) distance of ~ 1 pc. The authors assumed that the field occurrence rate of HJs is 1 percent (Wright et al. 2012), then adopted a planet radius $R_\mathrm{p} = 1.3\,R_\mathrm{J}$ and a typical period of 3.5 days, with a ten percent chance of geometric transit. This yielded an expected number of detected HJs within the sample to be 17. Given the non-detection of any HJ in their sample, the authors concluded that the HJ fraction in 47 Tuc is lower than in the field with high statistical significance.

However, a number of considerations have since been highlighted that reduce the significance of this finding. In the first instance, HJ incidence inferred from *Kepler* planets was estimated by Howard et al. (2012) to be 0.5 ± 0.1 percent. This fraction is lower than the ~ 1.2 percent inferred from an RV surveys by Marcy et al. (2005) and Wright et al. (2012). A slightly lower fraction of 0.89 ± 0.36 percent was inferred by Mayor et al. (2011), where HJs were defined to have masses $M_\mathrm{p} > 50\,M_\oplus$ and periods $P_\mathrm{orb} < 11$ days. This is approximately consistent with the value inferred by Howard et al. (2012). The *Kepler* detection rate may additionally be somewhat reduced by pipeline considerations such as the harmonic filter applied to remove periodic stellar activity, affecting transit recovery for planets with $P_\mathrm{orb} \lesssim 3$ days (Jenkins et al. 2010; Christiansen et al. 2015). Meanwhile, the statistics on the distribution of stellar properties and planet radii are challenging to recover from the RV data, for which many detections do not transit.

Masuda & Winn (2017) revisited the finding by GBG+00 using updated statistics for HJs around *Kepler* planets, including the distribution of radii and orbital periods. This is the most direct comparison that has been made between the surveyed 47 Tuc sample and the *Kepler* planets, finding an expected number of detections of $N_\mathrm{det} = 2.2^{+1.6}_{-1.1}$. This corresponds to an occurrence rate f_HJ of $0.43^{+0.07}_{-0.06}$ percent among *Kepler* targets with similar masses as the GBG+00 sample. Based on this estimate, we can therefore write the expected number of detections in 47 Tuc:

$$\langle N_\mathrm{det} \rangle \approx 2.2 \cdot \frac{f_\mathrm{HJ}}{4.3 \times 10^{-3}} \cdot \frac{N_\mathrm{samp}}{3.4 \cdot 10^4}, \tag{81}$$

where N_samp is the sample size and the stellar properties and sensitivity are similar to those of GBG+00. The corresponding probability of obtaining no detection is:

$$P_\mathrm{nd} = \binom{N_\mathrm{samp}}{0} (1 - f_\mathrm{det})^{N_\mathrm{samp}} \tag{82}$$

where

$$f_\mathrm{det} = \frac{\langle N_\mathrm{det} \rangle}{N_\mathrm{samp}}. \tag{83}$$

This yields $P_\mathrm{nd} \approx 0.11$ for $N_\mathrm{samp} = 3.4 \cdot 10^4$. Including the 21 920 stars surveyed in 47 Tuc by Weldrake et al. (2005), assuming comparable sensitivity, yields $P_\mathrm{nd} \approx 0.027$ – i.e. a marginally significant suppression with respect to the field population.

We can define the maximum f_HJ that is consistent with the constraints:

$$f_\mathrm{HJ,max} \approx 2 \cdot 10^{-3} \cdot 3.4 \cdot 10^4 \left(1 - P_\mathrm{nd,max}^{1/N_\mathrm{samp}}\right). \tag{84}$$

We will generally adopt $P_\mathrm{nd,max} = 0.05$ ($2\,\sigma$ significance) to give:

$$f_\mathrm{HJ,max} \approx 2 \cdot 10^{-3} \frac{10^5}{N_\mathrm{samp}}, \tag{85}$$

or $f_\mathrm{HJ,max} \approx 3.6 \times 10^{-3}$ for $N_\mathrm{samp} = 5.6 \cdot 10^4$. We will adopt the approximate expression equation 85 for the remainder of this work, with the caveat that future surveys must consider the sensitivity and stellar properties of their sample when computing significance of non-detections (as in Masuda & Winn 2017).

When comparing the observational constraints to the formation efficiency of HJs from our simulation, we will first adopt the extreme assumption that the number of massive planets per star $N_\mathrm{mp} = 1$ for every a_0 – i.e. that 100 percent of stars host planets with a given semi-major axis a_0. Our results can then be generalised by multiplying the fraction of planets that circularise in our simulations by the expected initial occurrence rate within some range δa_0 around a_0 – i.e. $\delta a_0 \cdot \mathrm{d}N_\mathrm{mp}/\mathrm{d}a_0$. We reconsider our findings in terms of inferred occurrence rates for field stars in Section 3.8.

3.3 Dynamical model

We model the dynamical evolution of 47 Tuc using the Monte Carlo code Mocca (Hypki & Giersz 2013; Giersz et al. 2013) with parameters motivated by the findings of Giersz & Heggie (2011). The model, including the density and velocity dispersion evolution, is discussed in Paper I. In brief, the model is initiated with $2 \cdot 10^6$ stars and an equal number of brown dwarfs and is evolved for 12 Gyr

to yield density and velocity distributions that consistent with the present day 47 Tuc.

In this model, we include a population of $2 \cdot 10^4$ 'migrating planets', which we use for benchmarking only, and not to compute the tidal outcomes for which we apply the analytic expressions derived in Section 2. The planets in the simulation are initiated with eccentricity $e_0 = 0.9$ and semi-major axes $a_0 = 5$ au, paired with stars drawn from the same IMF as single stars. While the stellar evolution is calculated using the code by Hurley et al. (2000, 2002) in Mocca, we do not include tidal forces in the orbital evolution of the binaries or planetary systems.

This population cannot be used to directly compute the eccentricity evolution and/or circularisation rates over the lifetime of 47 Tuc. The reasons for this are discussed in detail in Appendix D. In brief, the sampling framework in Mocca does not allow arbitrarily weak encounters in a given time-step. One therefore loses the encounters that yield small absolute changes in eccentricity $|\epsilon| \lesssim 0.05$, which are those in which we are most interested in this context. To capture such encounters accurately would require a much smaller time-step that would make the Monte Carlo simulations impracticable, essentially becoming an N-body simulation similar to that of HT17. We therefore simply show in Appendix D that the relative number of encounters resulting in a change of eccentricity of magnitude $|\epsilon|$ scales with $|\epsilon|^{-2}$ for sufficiently large $|\epsilon|$. This is as expected from the theoretical hyperbolic cross sections, as described in Section 2.3. The power-law index of -2 rather than -1 comes from the derivative of the cross section with respect to ϵ, since the cross section pertains to encounters of *at least* ϵ (or $\epsilon_{\rm thr}$). In conjunction with the comparison to the simulation results of HT17 presented in Section 2.11.2, this validates our analytic treatment such that we can apply it to our dynamical model.

3.4 Mass segregation

The rate of ionisation, circularisation and tidal destruction of a planet is dependent not only on the local velocity dispersion and density, but also the local mass function. The local mass function varies both temporally and spatially, which should be accounted for in computing the orbital evolution of the planets. We therefore define the local mass function numerically from the dynamical model.

At a given snapshot, we compute the percentiles in the mass distribution of stars within thirty logarithmically spaced radial bins between 0.1 pc and $10^{1.5}$ pc (i.e. with width 0.1 dex). The percentiles we compute are at intervals of five percent, except for the extreme upper and lower end where we include $1^{\rm st}$, $2^{\rm nd}$, $98^{\rm th}$ and $99^{\rm th}$ percentiles. We then numerically determine the derivative of the cumulative distribution function within the $1^{\rm st}$–$99^{\rm th}$ percentiles, interpolating to estimate the local mass function. We repeat this procedure at 100 Myr intervals up to the end of the simulation (12 Gyr).

The mass functions we compute are shown at 100 Myr, 1 Gyr and 10 Gyr in Figure 6. Initially the mass segregation only strongly influences high stellar masses and the inner regions (Figure 6a). Progressively more low mass stars are cleared from the centre of the cluster, eventually resulting in radically different mass functions in the inner and outer regions (Figure 6c).

When we compute the local encounter rates in our dynamical model, we adopt the mass function first at the closest snapshot and then the closest radial position. These mass functions are then numerically integrated over when calculating the relevant encounter rates for a given star.

3.5 Orbital integration

To compute the time-dependent evolution of the statistical outcomes for planets evolving in our model for 47 Tuc, we first draw a random subset of 1000 stars. Of these stars, 845 have masses $m_* < 0.88\,M_\odot$, which is the maximum mass that remains on the main sequence up to the 12 Gyr age of the cluster (see Section 3.2). For each of the stars in the sample we obtain the radial position and azimuthal and radial velocity, updated at 100 Myr intervals. We then obtain the local density and velocity dispersion averaged over an epicycle at each time-step. To do this, we fit an approximate analytic double power-law density profile:

$$\rho_* = \frac{M_{\rm s}}{4\pi a_{\rm s}^3} (r/a_{\rm s})^{-\alpha} (1 - r/a_{\rm s})^{\alpha-\beta} \tag{86}$$

to the stellar mass density of the cluster, where $M_{\rm s}$, $a_{\rm s}$, α and β are fitting constants. With these parameters, we construct a spherically symmetric potential using the `TwoPowerSphericalPotential` class of Galpy[1] (Bovy 2015). A number of alternative spherically symmetric profiles with fewer fitting parameters are possible, and allow faster integration of orbits. However, we adopt this density profile because it reliably reproduces the physical density profile in our Monte Carlo model (see Paper I). Due to the spherical symmetry, we are only interested in the radial oscillations in the stellar position. We therefore average σ_v and $n_{\rm tot}$ for a single epicycle.

With the averaged environmental properties we can then adopt the expressions in Section 2.11.1 to compute the evolution of a given outcome 'oc', $P_{\rm oc}$, by writing:

$$P_{\rm oc}(t + \Delta t) = P_{\rm oc}(t) + \Delta t \cdot \dot{P}_{\rm oc}(t). \tag{87}$$

Note that we can choose a time-step that is smaller than that which we update the orbital solutions in our dynamical model (100 Myr). For each star, we compute the probability over 3000 equal time-steps up to 12 Gyr. For computing the tidal rates, we will assume the initial planet eccentricity is $e_0 = 0.1$, which is a typical value for the eccentricity of planets forming in hydrodynamic simulations of protoplanetary discs (e.g. Bitsch & Kley 2010; Dunhill et al. 2013; Ragusa et al. 2018).

3.6 Time evolution of outcome probabilities

The results of computing the outcome probabilities according to equation 87 are shown in Figure 7, for ionisation (blue), circularisation (red) and tidal destruction (yellow-green). We find that for initial semi-major axis $a_0 = 1$ au HJ production is efficient, producing circularised planet at a yield of $P_{\rm circ} \sim 0.02$. If 100 percent of systems hosted planets at these separations, such high numbers of HJs would be in tension with the observed absence of short period companions, discussed in Section 3.2. However, as discussed in Section 3.8, this is not expected given field star occurrence rates. In addition, as the initial semi-major axis of the planet increases, this efficiency decreases. This is due to increasing ionisation and tidal destruction rates. We explore this further in terms of the final outcomes as follows.

[1] `http://github.com/jobovy/galpy`

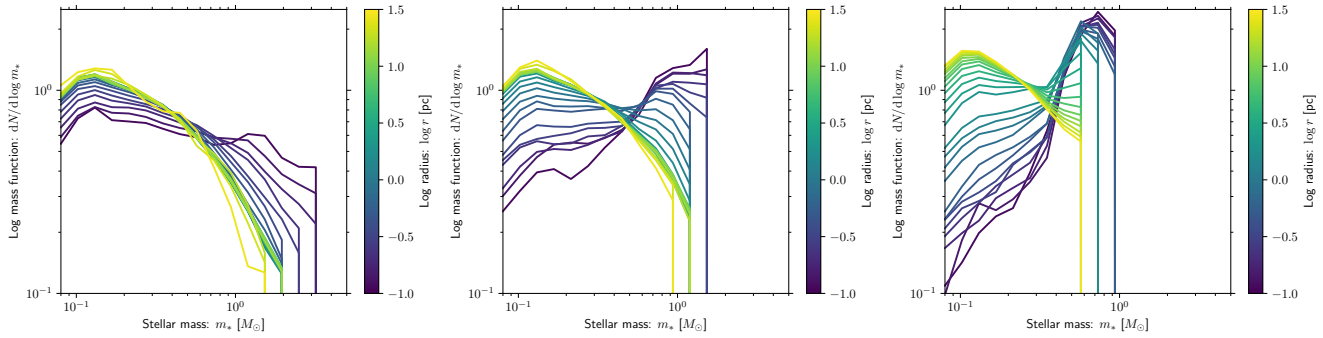

(a) 100 Myr (b) 1 Gyr (c) 10 Gyr

Figure 6. Stellar mass function binned by three dimensional radius within the cluster, with bin size 0.1 dex, as shown by the colour bar. The results are shown for the stellar population in our dynamical model at 100 Myr (Figure 6a), 1 Gyr (Figure 6b) and 10 Gyr (Figure 6c).

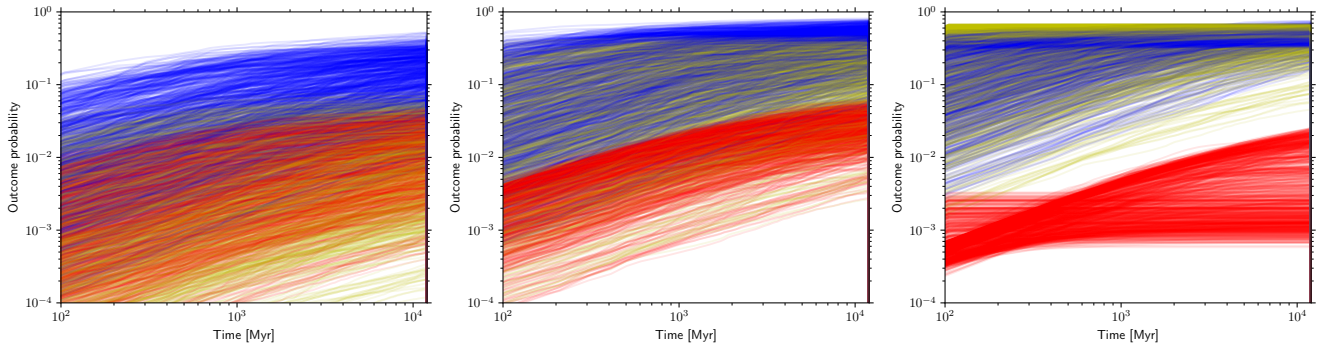

(a) $a_0 = 1$ au (b) $a_0 = 5$ au (c) $a_0 = 25$ au

Figure 7. Evolution of the probability of the different outcomes for a planet evolving in 47 Tuc. Each line corresponds to a single star in a subset of 845 stars with masses $m_* < 0.88\,M_\odot$ in our dynamical model. Probabilities for ionisation or exchange (blue lines), circularisation (red lines) or tidal destruction (yellow-green lines). Results are shown for initial planet semi-major axes $a_0 = 1$ au (Figure 7a), 5 au (Figure 7b) and $a_0 = 25$ au (Figure 7c). When the lines become practically horizontal (constant in time), the probabilities are 'locked in', in that there is very little chance of a planet having escaped all of the three possible outcomes.

3.7 Final outcomes

3.7.1 Projection averaging

We are interested in quantifying the observable dependence on the outcomes as a function of projected separation d from the centre of the cluster. In two dimensions, we can geometrically average the outcome probabilities $P_{\rm oc}$:

$$\langle P_{\rm oc}\rangle_{\rm 2D}(d) = \frac{1}{n_d}\sum_{r_i>d}\frac{P_{{\rm oc},i}}{r_i}\frac{d}{\sqrt{r_i^2-d^2}} \tag{88}$$

where

$$n_d = \sum_{r_i>d}\frac{d}{r_i\sqrt{r_i^2-d^2}}. \tag{89}$$

and $P_{{\rm oc},i}$ is the outcome probability for each star i at three dimensional radius r_i.

3.7.2 Dependence on final projected radial position

We show the results of computing equation 88 for varying projected separation d in our simulation at $t = 12$ Gyr in Figure 8. We also show the approximate upper limit for the fraction of HJs inferred from the aggregated sample of GBG+00 and Weldrake et al. (2005) – this should be understood as the upper limit if the planet occurrence was 100 percent. Thus across all a_0 au the rate of HJ production is close to this upper limit if occurrence rates are significantly samller than this (e.g. 10 percent). We explore the dependence on a_0 in greater detail in Section 3.7.4.

It is clear from Figure 8 that the final outcomes are practically independent of the projected separation from the cluster centre. This is somewhat suprising due to the strong dependence on the rates of ionisation, circularisation and tidal destruction on local density and velocity dispersion. In fact, this finding also applies to the final position in three dimensions, and is not a result of our projected separation averaging. This suggests that the origin of this finding is that most outcomes are 'locked-in' early during the dynamical evolution, and dynamical mixing subsequently washes out any trends. We confirm this hypothesis as follows.

3.7.3 Dependence on initial radial position

We wish to examine whether the initial radial location of a star-planet system in the cluster is a better predictor of the outcome for planets than the final position. We therefore consider the final outcome probabilities versus the initial radius r_0 in Figure 9. We

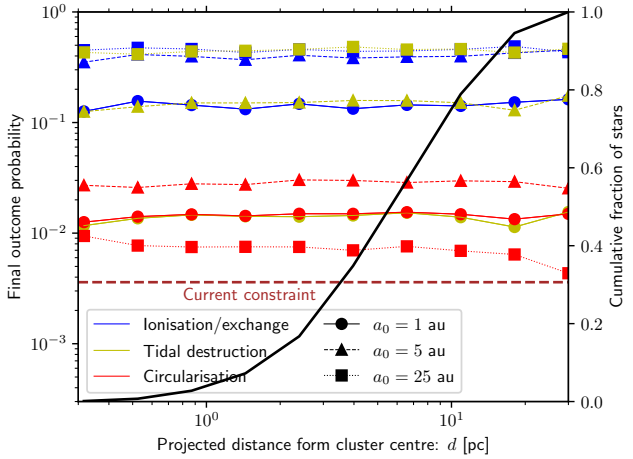

Figure 8. Statistical outcomes for planets evolving in 47 Tuc as a function of the final projected separation from the cluster centre after 12 Gyr of evolution. Results are shown for a planet initially at $a_0 = 1$ au, 5 au and 25 au. Ionisation/exchange probabilities are shown in blue, tidal destruction in yellow-green, circularisation in red. The dashed brown line is the estimated 2σ constraint on the total fraction of HJs in the aggregate samples of GBG+00 and Weldrake et al. (2005) (see discussion in Section 3.2). This constraint can be compared with the yields per planet (red lines) by multiplying by the expected number of planets per star. The solid black line shows the cumulative fraction of the sample within each projected separation.

find that the final outcome is indeed a strong function of the initial position in the cluster. The previous result that there is no strong dependence of outcomes on the final position in the cluster is therefore a result of dynamical mixing.

In particular, for all a_0 the sum of all outcomes – i.e. the probability that the environment significantly influences the star-planet – decreases with increasing radius. This is expected because the stellar density is greater in the inner regions, and therefore stellar encounters are more frequent at smaller r_0.

There are also some qualitative changes in the radial dependence of the fractional outcomes with the initial semi-major axis. For small $a_0 = 1$ au (Figure 7a), all outcomes behave similarly, with probabilities declining with r_0. However, as a_0 increases, tidal destruction begins to dominate over circularisation in the central regions. This results in declining HJ formation rates with decreasing r_0, seen clearly in Figure 7c. This is due to the large perturbation rate (or γ value, equation 35), which results in small $l_{\rm max}$ and large $f_{\rm td}$ (see Section 2.7 and 2.9) – i.e. a planet cannot circularise without already undergoing tidal disruption. HJ formation is therefore inefficient for planets at large a_0 and stars born in the inner regions of globular clusters.

3.7.4 *Semi-major axis dependence*

In Figure 10 we show the variation of the final outcome probabilities as a function of initial semi-major axis a_0. We choose the values averaged at projected separation $d = 1$ pc, although in practice this choice makes little difference, as shown in Figure 8. We find that the fraction of planets that experience tidal destruction increases with a_0, and is the most likely outcome for $a_0 \gtrsim 30$ au. For $a_0 \gtrsim 50$ au, the frequency of HJ production decreases below the upper limit constraint for $f_{\rm HJ}$ aggregated across the surveys of GBG+00 and Weldrake et al. (2005). Thus even a 100 percent occurrence rate of planets at these semi-major axes would not be expected to yield any HJs in these samples. The slight increase in the fraction of circularised planets at large a_0 is due to the decrease in the ionisation rate compared with the perturbation rate ($\Gamma_{\rm ion} \propto a_0$ while $\Gamma_{\rm per}^{\rm (hyp)} \propto a_0^{3/2}$), which is related to the inefficiency of ionisation in high velocity dispersion environments.

3.7.5 *Stellar mass dependence*

When considering future surveys of globular clusters, we may be interested in whether the outcome probabilities are dependent on the stellar mass. We show the probabilities for semi-major axis $a_0 = 5$ au in Figure 11 (the results are similar for varying a_0). We find that there is only a very weak dependence of the different outcomes across the relevant range of stellar masses. This is because the differences between ionisation and perturbation cross sections is only moderately dependent on the stellar mass via the ratio with the local stellar mass function. Mass segregation further suppresses this difference by yielding encounters that preferentially have order unity mass ratio. In conclusion, we do not expect the mass function of surveyed stars to strongly influence the occurrence rate of HJs. However, this does not apply to detectability (see discussion by Masuda & Winn 2017).

3.8 Initial planet population

3.8.1 *Massive planet occurrence*

In order to interpret our findings, we need to convert the efficiency at which planets are converted into HJs into an occurrence rate of HJs *per star*. To do this we must appeal to field star planet occurrence rates as a function of a_0, $\mathrm{d}N_{\rm mp}/\mathrm{d}\log a_0$. We have previously implicitly assumed that one hundred percent of stars host a planet at each initial semi-major axes a_0, or $\mathrm{d}N_{\rm mp}/\mathrm{d}\log a_0 = \delta(a_0')$ where δ is the Dirac delta distribution and a_0' is any value of a_0 we have adopted. We now consider empirical constraints on the true occurrence rates of giant planets.

Particularly useful in this context are the results of the *Gemini Planet Imager Exoplanet Survey* (GPIES) presented by Nielsen et al. (2019). This survey is sensitive to planets/brown dwarfs with semi-major axes $3\,\mathrm{au} \lesssim a \lesssim 100$ au and masses $3\,M_{\rm J} \lesssim M_{\rm p} \lesssim 100\,M_{\rm J}$. The authors extrapolate their findings to estimate the frequency of planets with $0.03\,\mathrm{au} \lesssim a \lesssim 100$ au and $1\,M_{\rm J} \lesssim M_{\rm p} \lesssim 13\,M_{\rm J}$ around solar mass stars, combining with the previous estimates of Cumming et al. (2008) and Fernandes et al. (2019) for closer-in massive planets (see Figure 18 of Nielsen et al. 2019). The resultant total per star occurrence rate for massive planets in this range is $N_{\rm mp} \sim 0.1$.

In order to convert our results to an expected occurrence rate of HJs in 47 Tuc, we must make some assumptions about how the occurrence rate varies with semi-major axis ($\mathrm{d}N_{\rm mp}/\mathrm{d}\log a$). Interpreting the occurrence rates of massive planets in the field is not straight forward in this context. This is not only because definitions of the occurrence rates depend on the mass range considered (and physical/observational covariance with a), but also because we work on the premise that some fraction of planets migrate by HEM. In this case, the occurrence rates as a function of semi-major axis a, is by definition not the same as that of the initial semi-major axis a_0 (see Winter & Alexander 2021, for example).

For the above reasons, we make a simplified estimate for the form of $\mathrm{d}N_{\rm mp}/\mathrm{d}\log a$, with the caveat that this form remains uncertain. Based on the findings of Nielsen et al. (2019), $\mathrm{d}N_{\rm mp}/\mathrm{d}\log a$ is not well constrained at large separations. In the approximately solar

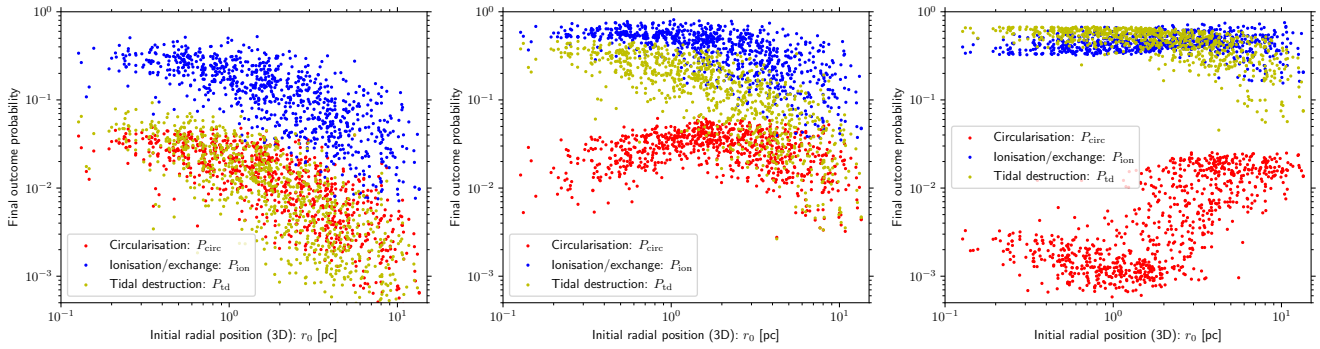

(a) $a_0 = 1$ au (b) $a_0 = 5$ au (c) $a_0 = 25$ au

Figure 9. Dependence of the final outcome probability on the initial three dimensional radial position. We show results for initial semi-major axes $a_0 = 1$ au (Figure 9a), 5 au (Figure 9b) and 25 au (Figure 9c). The blue points show the probability that a planet has undergone ionisation, yellow-green for tidal destruction and red for circularisation.

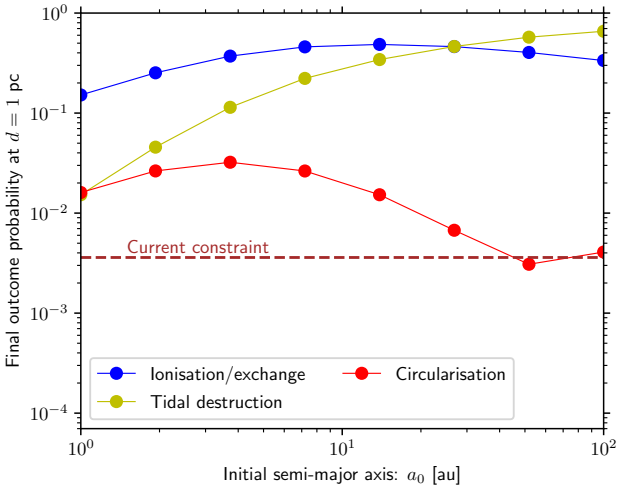

Figure 10. Probability of outcomes for a planetary system evolving within our dynamical model of 47 Tuc as a function of the initial semi-major axis a_0. A projected average probability at $d = 1$ pc is adopted, although the results are not strongly dependent on this choice (Figure 8). The points show the discrete values of a_0 that are adopted. Blue lines are for ionisation/exchange, yellow-green for tidal destruction and red for circularisation. The dashed brown line shows the 2σ constraint on the HJ fraction from the aggregated GBG+00 and Weldrake et al. (2005) samples, which can be compared with final outcome probabilities by multiplying by the per star occurrence rates.

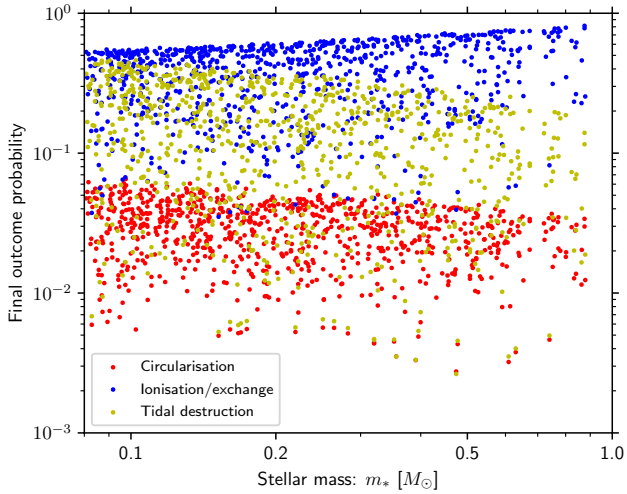

Figure 11. The distribution of outcome probabilities for planets around 845 randomly selected stars of mass $m_* < 0.88\,M_\odot$ in our dynamical model as a function of m_* after 12 Gyr. The initial semi-major axis in this case is $a_0 = 5$ au. The outcomes considered are ionisation/exchange of the planet (blue points), circularisation (red points), and tidal destruction (yellow-green points).

mass stellar sample, the detected companion with the greatest semi-major axis has $a \sim 30$ au (projected separation 23.65 ± 0.08 au). The results therefore appear broadly consistent with an occurrence rate that is uniform in $\log a$, truncated outside of 30 au. We impose an inner truncation radius of 1 au, motivated by the fact that Fernandes et al. (2019) find very few planets with $M_{\rm p} > 1\,M_{\rm J}$ inside this separation (see their Figure 1). We then normalise over this range to give an overall occurrence rate of $N_{\rm mp} = 0.1$:

$$\frac{{\rm d}N_{\rm mp}}{{\rm d}\log a_0} = \begin{cases} 0.0677 & 1\,{\rm au} < a_0 < 30\,{\rm au} \\ 0 & \text{otherwise} \end{cases} \tag{90}$$

Visually considering such a mass function on the top panels of Figure 18 of Nielsen et al. (2019), we see that equation 90 would remain broadly consistent with the posterior distributions inferred by Cumming et al. (2008), Fernandes et al. (2019) and Nielsen et al. (2019) for 1 au$< a <$ 30 au.

3.8.2 *Application to 47 Tuc*

We now compute the expected number of HJs forming in 47 Tuc:

$$f_{\rm HJ} = \int P_{\rm HJ}(a_0) \cdot \frac{{\rm d}N_{\rm mp}}{{\rm d}\log a_0}\,{\rm d}\log a_0. \tag{91}$$

To compute this occurrence rate, we use the numerical results for the probability of a given planet with initial semi-major axis a_0 becoming a HJ, $P_{\rm HJ}(a_0)$, shown as the red line in Figure 10. Adopting the occurrence rate of massive planets in semi-major axis space as defined by equation 90, we obtain $f_{\rm HJ} = 2.2 \times 10^{-3}$. This remains consistent with the constraint $f_{\rm HJ,max} \approx 3.6 \times 10^{-3}$ inferred in Section 3.2 for the combined samples of GBG+00 and Weldrake et al. (2005).

Our findings therefore suggest that in order to determine whether the planets in globular clusters are significantly different to the field, transit surveys with sample size $\gtrsim 10^5$ *(based on equation 85) at the survey sensitivity of Gilliland et al. (2000) are required.* Alternatively, smaller sample sizes with greater survey sensitivities could in principle rule out a more abundant lower mass planet population. This latter possibility has the caveat that the tidal distortion (or Q-factor) is dependent on the planet properties. While the rate of tidal circularisation is dependent on the apsidal motion constant k_p and tidal lag time τ_p (e.g. equation 11), the maximum SLR l_max (equation 47) is only weakly dependent on these assumed constants. Thus our results should be a reasonable estimate of the outcome probabilities of (massive) planets in general. Nonetheless, future application to lower mass planets should consider variations in these constants, as well as the closest approach distance required for tidal disruption (Section 2.9).

3.9 Future survey ramifications

We can ask what the consequences of detection or non-detection of HJs in future surveys of 47 Tuc would be, both for the local planet population and more generally for the formation pathways of HJs in the field. In this section, we summarise the consequences of future detection (Section 3.9.1) or non-detection (Section 3.9.2) of HJs in globular clusters. We consider in greater detail each possible isolated formation mechanism in Sections 3.9.3, 3.9.4 and 3.9.5.

3.9.1 *Detection in a large/sensitive survey*

Detecting the first HJ in a globular cluster is a tantalizing prospect. Such an object would in itself represent the outcome of planet formation in an environment completely different from local star forming regions. However, from a statistical perspective, a single discovery constraining the population of HJs to an occurrence rate $f_\mathrm{HJ} \sim 10^{-3}$ would not distinguish between a range of interpretations. It could mean that normal HJ formation is via a mechanism that is unaffected by dynamical encounters (such as disc-induced migration, see Section 3.9.5), or it could mean that these HJs were created by scattering of a population of wider planets that are similar to that of the solar neighbourhood. Future follow-up on such a discovery may offer ways to distinguish between these possibilities.

3.9.2 *Non-detection in a large/sensitive survey*

Statistically, the most interesting constraints would originate from non-detection of any HJs in a large and sensitive future transit survey, constraining the massive ($M_\mathrm{p} \gtrsim 1\,M_\mathrm{J}$) HJ occurrence rate to $f_\mathrm{HJ,max} < 2.2 \times 10^{-3}$ (or larger if greater sensitivity than the survey of GBG+00). *Non-detection in such a sample would suggest both a paucity of massive planets at wide separations relative to the solar neighbourhood and that any formation mechanism producing HJs in low density environments does not operate.*

In the case of non-detection, the general pathway for HJ formation must be one which can be viably disrupted in a dense environment. The formation pathways that should most obviously be disrupted would be those of HEM (see Sections 3.9.3 and 3.9.4). In this case, non-detection in a large/sensitive transit sample could indicate that HEM is the origin of HJs in the field. However, LEM migration mechanisms may also be suppressed in a low metallicity environment (see Section 3.9.5). Thus non-detection could also imply that planet formation is completely suppressed across a large dynamical range in semi-major axis. We discuss each of the isolated HJ formation mechanisms in further detail as follows.

3.9.3 *Planet-planet scattering*

Planet-planet scattering within isolated planetary systems has been suggested as a possible origin of the eccentricity excitation required to produce HJs via HEM (Rasio & Ford 1996; Carrera et al. 2019). Whether or not this formation channel produces enough HJs to explain the observed occurrence rates depends sensitively on the initial stability of planetary systems. For example, it remains unclear whether *Kepler* multiple systems statistically 'pile-up' close to the stability limit (Pu & Wu 2015; Yee et al. 2021), which is a necessary measurement to quantify the frequency of chaotic dynamical decay.

To gain an intuition as to how HJ formation via planet-planet scattering may proceed in the context of globular clusters we consider a simple thought experiment. We consider a planet excited by internal scattering to a SLR $l < l_\mathrm{age}$, as required for the planet to circularise over its lifetime. This planet is then also subject to the usual encounters in a high density environment. Thus it is still unable to circularise if $l > l_\mathrm{max}$, as depicted in Figure 3. Therefore, even HJ formation via planet-planet scattering is subject to the same suppression by tidal disruption as HJ formation via external encounters. The difference in the planet-planet scattering case is that the condition $l < l_\mathrm{max}$ may be reached earlier than it would be relying on encounters alone. This may reduce the frequency of ionisation for such a planetary system. To first order, we can ignore ionisation and estimate the suppression of HJ formation via planet-planet scattering using the ratio of the yellow-green line to the sum of the red and yellow-green lines in Figure 10. If such HJs originate from initial semi-major axes $a_0 \gtrsim 1$ au, then the majority are unable to migrate.

3.9.4 *Outer companions*

Some fraction of HEM may be induced via Kozai-Lidov oscillations within binary/multiple planet systems (Kozai 1962; Lidov 1962; Naoz 2016; Hamers & Lai 2017). Indeed, a number of studies have suggested that massive planets/HJs preferentially have outer companions (Ngo et al. 2016; Fontanive et al. 2019; Belokurov et al. 2020). Unlike in the planet-planet scattering case discussed above, outer companions may dominate the eccentricity evolution of planets during circularisation rather than the influence of more distant star-star encounters. We may therefore naturally ask whether we expect Kozai-Lidov oscillations to produce HJs similarly in very high density environments such as 47 Tuc.

Our findings indicate that if the outer companion which would in isolation be giving rise to Kozai-Lidov oscillations is at a separation > 10 au, then the eccentricity oscillations would be interrupted by tidal disruption or ionisation (Figure 10). From Figure 7, we see that this disruption can occur on time-scales that are $\lesssim 100$ Myr, possibly shorter than those required to produce a circularised HJ. We conclude that Kozai-Lidov may be suppressed in 47 Tuc-like environments, although this process requires further exploration with future numerical experiments.

3.9.5 *Low eccentricity migration*

Throughout this work, we have implicitly assumed that LEM through the primordial protoplanetary disc (Lin et al. 1996) is not the origin of HJs. If HJs do in fact originate from migration within

a disc, then there is no reason to assume this mechanism should be suppressed by dynamical perturbations. In dense environments, the massive outer planets that undergo eccentricity fluctuations could in principle result in tidal destruction, which would also presumably destroy the inner HJ. However, such massive outer systems would frequently be ionised rather than tidally destroyed. For outer planets with $a_0 \lesssim 30$ au, this would not destroy the majority of HJs that form via LEM. Therefore, non-detection of HJs in future transit surveys of globular clusters would imply that LEM can only be the origin of the field HJs if the low metallicity environment suppresses their formation and/or migration. Thus, constraints on $f_{\rm HJ}$ from future surveys would supply strict conditions on planet formation across a wide dynamical range in semi-major axis.

3.10 Caveats for outcome probabilities

We have presented an analytic approach to computing the rates of circularisation, destruction and ionisation in dense stellar environments. Our prescription is useful for quick computation and application to dynamical models. However, a number of considerations may alter the true outcome frequencies with respect to predictions from our analytic approach. Some factors that may alter the rates of HJ formation include, but are not limited to:

- *Systems of planets*: Our models apply to single planet systems. However, we have not directly considered how systems of planets may (mutually) alter eccentricity evolution in such systems. This may increase or decrease the frequencies of the various outcomes we have considered in this work. However, we would generally expect the same suppression of HJ formation due to dynamical encounters, as we discuss in Section 3.9.3.
- *Binary fraction*: We have assumed an initial binary fraction based on that adopted by Giersz & Heggie (2011), which was necessarily low to reproduce the observed present-day density profile. We do not here attempt to constrain this fraction. If the initial binary fraction was high, then this might result in a larger typical interaction cross section for encounters (e.g. Li et al. 2020), and interplay with Kozai-Lidov oscillations as discussed in Section 3.9.4.
- *Limits of the analytic treatment*: We have discussed that we generally assume that hyperbolic encounters dominate the eccentricity evolution of planets. This is true only for sufficiently large velocity dispersion σ_v and/or semi-major axis a such that typical encounter velocities are $v_\infty \gtrsim v_{\rm orb}$, the orbital velocity. In addition, in the the extreme eccentricity limits ($e \to 0, 1$), the perturbation cross section may be dominated by higher order (octopole) terms, which we do not treat in this work. For very extreme eccentricities, external perturbations may be more frequent than suggested by our equations.
- *Dynamical model uncertainties*: As discussed in Paper I, a number of possible physical mechanisms – such as tidal shocks (Gnedin et al. 1999) or the formation black hole subsystems (Breen & Heggie 2013; Giersz et al. 2019) – may influence the dynamical evolution of 47 Tuc. Such mechanisms could dynamically heat the cluster, and therefore the initial core density (in which we are are most interested) may have been larger than we have assumed. If the velocity dispersion was initially larger than in our model, we would expect fewer ionisations relative to circularisation and tidal destruction. Meanwhile, higher densities favour greater numbers of planets undergoing tidal destruction with respect to circularisation.

4 CONCLUSIONS

In this work, we explore the apparent absence of close-in sub-stellar companions in the globular cluster 47 Tuc from a theoretical perspective. In particular, we are interested in how HEM of (potential) HJs is influenced by dynamical encounters in dense stellar environments. This process requires numerous close passages with the host star, over which the tides raised in the planet lead to orbital circularisation. Planets in dense environments experience eccentricity perturbations during the time they are undergoing circularisation. Eccentricity perturbations can either excite large eccentricities which promote tidal interactions with the host star, or reduce the eccentricity to curtail such interactions. The net effect of this behaviour in a dense environment can be determined statistically, such that the overall outcome of HEM in globular clusters is predictable given an initial planet population.

To quantify the efficiency of HJ production via HEM in dense stellar environments, we develop a theoretical prescription for the evolution of the orbital eccentricity of a planet subject to stellar encounters in dense environments. In order for a planet to circularise, the rate of this eccentricity perturbation must be slower than the rate of tidal circularisation. Using this principle, we derive a maximum semi-latus rectum $l_{\rm max}$ along which a planet can circularise at a given density (equation 47). Planets can only circularise when $l < l_{\rm max}$, while in isolation they may circularise if $l < l_{\rm age}$ (the semi-latus rectum for which a planet circularises during the age of the star). This situation is depicted in Figure 3, which shows the outcome of numerical experiments tracking the evolution of semi-major axis and eccentricity for planets experiencing both dynamical perturbations and circularising tides. For sufficiently small $l_{\rm max} < l_{\rm age}$, planets that may have circularised in isolation instead undergo such close passages with their host star as to experience tidal disruption rather than circularisation. Thus, above some critical density approximated by equation 49, HJ formation in dense environments becomes inefficient. We quantify the fraction of would-be HJs that are tidally disrupted, coupling this with the rate at which eccentricities sufficient to circularise are excited. Combining our prescription with previously derived cross sections for ionisation, we derive analytic expressions for the fractions of planets that undergo ionisation, tidal disruption and circularisation in dense stellar environments. We find good agreement between these expressions and the numerical experiments of Hamers & Tremaine (2017). These expressions demonstrate that HJ formation is inefficient at extremely high densities, and could explain the apparent discrepancy between the occurrence rates of HJs in M67 (Brucalassi et al. 2016) and 47 Tuc (Gilliland et al. 2000; Weldrake et al. 2005).

Having validated our analytic expressions, we apply them to a Monte Carlo dynamical model of 47 Tuc using the Mocca code (Giersz 1998, 2001). We demonstrate that the efficiency of HJ formation in dense stellar environments is a strong function of the initial semi-major axis. The absence of HJs found in 47 Tuc therefore has consequences for the planet formation rates in general. We find that, assuming the same initial occurrence rate of massive planets in 47 Tuc as for field stars as a function of semi-major axis, the expected HJ occurrence rate is $f_{\rm HJ} \approx 2.2 \times 10^{-3}$, which remains consistent with current constraints ($f_{\rm HJ,max} \approx 3.6 \times 10^{-3}$). The HJ occurrence rate is sensitive to the initial planet occurrence rate at semi-major axis $a_0 \sim 1{-}30$ au. Thus, applying our theoretical framework, future transit surveys have the capacity to robustly determine the efficiency of planet formation in globular clusters. In order to rule out a occurrence rates of planets in globular clusters similar to the field, a transit survey sample size of $\gtrsim 10^5$ stars is

required at a similar sensitivity as that of Gilliland et al. (2000). Alternatively, higher sensitivity surveys may probe the prevalence of lower mass planets.

In this work and in Paper I we have made the case for future efforts in searching for short period sub-stellar companions in globular clusters. Present constraints on their occurrence tells us little about the physics of star and planet formation in such environments. However, with a sufficiently large sample size, searches have the potential to constrain:

(i) the environmental dependence of the sub-stellar IMF, due to the expected fraction of tidal brown dwarf captures (Paper I);

(ii) the occurrence rate of massive planets with respect to the solar neighbourhood, due to the role of encounter-induced migration in generating HJs from planets in initially wider orbits (this work).

We thus conclude that there remains much to learn from future searches for planets in globular clusters by applying the mapping of the initial sub-stellar populations to the short-period companion fractions we have presented in this work.

ACKNOWLEDGEMENTS

We thank the anonymous referee for their careful reading that improved the clarity of this manuscript. AJW acknowledges funding from an Alexander von Humboldt Stiftung Postdoctoral Research Fellowship. CJC acknowledge support from the STFC consolidated grant ST/S000623/1. This work has also been supported by the European Union's Horizon 2020 research and innovation programme under the Marie Sklodowska-Curie grant agreement No 823823 (DUSTBUSTERS). GR acknowledges support from the Netherlands Organisation for Scientific Research (NWO, program number 016.Veni.192.233) and from an STFC Ernest Rutherford Fellowship (grant number ST/T003855/1). This project has received funding from the European Research Council (ERC) under the European Union's Horizon 2020 research and innovation programme (grant agreement No 681601) and been supported by the DISCSIM project, grant agreement 341137 funded by the ERC under ERC-2013-ADG.

REFERENCES

Adams F. C., Laughlin G., 2006, ApJ, 649, 1004
Adams F. C., Hollenbach D., Laughlin G., Gorti U., 2004, ApJ, 611, 360
Alexander M. E., 1973, Ap&SS, 23, 459
Bailey J. I., Mateo M., White R. J., Shectman S. A., Crane J. D., 2018, MNRAS, 475, 1609
Baruteau C., et al., 2014, in Beuther H., Klessen R. S., Dullemond C. P., Henning T., eds, Protostars and Planets VI. p. 667 (arXiv:1312.4293), doi:10.2458/azu_uapress_9780816531240-ch029
Belokurov V., et al., 2020, MNRAS, 496, 1922
Bergbusch P. A., Vandenberg D. A., 1992, ApJS, 81, 163
Bitsch B., Kley W., 2010, A&A, 523, A30
Bonnell I. A., Clarke C. J., Bate M. R., Pringle J. E., 2001, MNRAS, 324, 573
Boss A. P., 2002, ApJ, 567, L149
Bovy J., 2015, ApJS, 216, 29
Breen P. G., Heggie D. C., 2013, MNRAS, 432, 2779
Breslau A., Steinhausen M., Vincke K., Pfalzner S., 2014, A&A, 565, A130
Brucalassi A., et al., 2016, A&A, 592, L1
Carrera D., Raymond S. N., Davies M. B., 2019, A&A, 629, L7
Christiansen J. L., et al., 2015, ApJ, 810, 95
Cumming A., Butler R. P., Marcy G. W., Vogt S. S., Wright J. T., Fischer D. A., 2008, PASP, 120, 531
Damasso M., et al., 2020, A&A, 642, A133
Davies M. B., Sigurdsson S., 2001, MNRAS, 324, 612
Dawson R. I., Johnson J. A., 2018, ARA&A, 56, 175
Donati J. F., et al., 2020, MNRAS, 491, 5660
Dong J., et al., 2021, ApJ, 920, L16
Dunhill A. C., Alexander R. D., Armitage P. J., 2013, MNRAS, 428, 3072
Eggleton P. P., Kiseleva L. G., Hut P., 1998, ApJ, 499, 853
Ercolano B., Clarke C. J., 2010, MNRAS, 402, 2735
Facchini S., Clarke C. J., Bisbas T. G., 2016, MNRAS, 457, 3593
Fernandes R. B., Mulders G. D., Pascucci I., Mordasini C., Emsenhuber A., 2019, ApJ, 874, 81
Fontanive C., Rice K., Bonavita M., Lopez E., Mužić K., Biller B., 2019, MNRAS, 485, 4967
Ford E. B., Rasio F. A., 2008, ApJ, 686, 621
Fortney J. J., Dawson R. I., Komacek T. D., 2021, Journal of Geophysical Research (Planets), 126, e06629
Fregeau J. M., Cheung P., Portegies Zwart S. F., Rasio F. A., 2004, MNRAS, 352, 1
Fregeau J. M., Chatterjee S., Rasio F. A., 2006, ApJ, 640, 1086
Gebhardt K., Pryor C., Williams T. B., Hesser J. E., 1995, AJ, 110, 1699
Giersz M., 1998, MNRAS, 298, 1239
Giersz M., 2001, MNRAS, 324, 218
Giersz M., Heggie D. C., 2011, MNRAS, 410, 2698
Giersz M., Heggie D. C., Hurley J. R., Hypki A., 2013, MNRAS, 431, 2184
Giersz M., Askar A., Wang L., Hypki A., Leveque A., Spurzem R., 2019, MNRAS, 487, 2412
Gilliland R. L., et al., 2000, ApJ, 545, L47
Gnedin O. Y., Lee H. M., Ostriker J. P., 1999, ApJ, 522, 935
Goldreich P., Soter S., 1966, Icarus, 5, 375
Goldreich P., Tremaine S., 1980, ApJ, 241, 425
Guillochon J., Ramirez-Ruiz E., Lin D., 2011, ApJ, 732, 74
Hamers A. S., Lai D., 2017, MNRAS, 470, 1657
Hamers A. S., Tremaine S., 2017, AJ, 154, 272
Haworth T. J., Clarke C. J., Rahman W., Winter A. J., Facchini S., 2018, MNRAS, 481, 452
Heggie D. C., 1975, MNRAS, 173, 729
Heggie D. C., Rasio F. A., 1996, MNRAS, 282, 1064
Hills J. G., Dissly R. W., 1989, AJ, 98, 1069
Howard A. W., et al., 2012, ApJS, 201, 15
Hurley J. R., Pols O. R., Tout C. A., 2000, MNRAS, 315, 543
Hurley J. R., Tout C. A., Pols O. R., 2002, MNRAS, 329, 897
Hut P., 1981, A&A, 99, 126
Hut P., 1982, A&A, 110, 37
Hut P., Bahcall J. N., 1983, ApJ, 268, 319
Hypki A., Giersz M., 2013, MNRAS, 429, 1221
Jackson B., Greenberg R., Barnes R., 2008, ApJ, 678, 1396
Jenkins J. M., et al., 2010, in Radziwill N. M., Bridger A., eds, Society of Photo-Optical Instrumentation Engineers (SPIE) Conference Series Vol. 7740, Software and Cyberinfrastructure for Astronomy. p. 77400D, doi:10.1117/12.856764
Johnson J. A., Aller K. M., Howard A. W., Crepp J. R., 2010, PASP, 122, 905
Johnstone D., Hollenbach D., Bally J., 1998, ApJ, 499, 758
Kozai Y., 1962, AJ, 67, 591
Lega E., et al., 2021, A&A, 646, A166
Li D., Mustill A. J., Davies M. B., 2020, MNRAS, 499, 1212
Lidov M. L., 1962, Planet. Space Sci., 9, 719
Lin D. N. C., Papaloizou J., 1986, ApJ, 309, 846
Lin D. N. C., Bodenheimer P., Richardson D. C., 1996, Nature, 380, 606
Marcy G., Butler R. P., Fischer D., Vogt S., Wright J. T., Tinney C. G., Jones H. R. A., 2005, Progress of Theoretical Physics Supplement, 158, 24
Masuda K., Winn J. N., 2017, AJ, 153, 187
Mayor M., Queloz D., 1995, Nature, 378, 355
Mayor M., et al., 2011, arXiv e-prints, p. arXiv:1109.2497
McCormac J., et al., 2020, MNRAS, 493, 126
Miret-Roig N., et al., 2021, Nature Astronomy
Naoz S., 2016, ARA&A, 54, 441
Ngo H., et al., 2016, ApJ, 827, 8

Nielsen E. L., et al., 2019, AJ, 158, 13
Ostriker E. C., 1994, ApJ, 424, 292
Paulson D. B., Yelda S., 2006, PASP, 118, 706
Pinte C., Dent W. R. F., Ménard F., Hales A., Hill T., Cortes P., de Gregorio-Monsalvo I., 2016, ApJ, 816, 25
Pu B., Wu Y., 2015, ApJ, 807, 44
Ragusa E., Rosotti G., Teyssandier J., Booth R., Clarke C. J., Lodato G., 2018, MNRAS, 474, 4460
Rasio F. A., Ford E. B., 1996, Science, 274, 954
Rice M., Wang S., Laughlin G., 2022, Origins of Hot Jupiters from the Stellar Obliquity Distribution (arXiv:2201.11768)
Rodet L., Su Y., Lai D., 2021, ApJ, 913, 104
Salpeter E. E., 1955, ApJ, 121, 161
Santos N. C., Israelian G., Mayor M., 2001, A&A, 373, 1019
Shara M. M., Hurley J. R., Mardling R. A., 2016, ApJ, 816, 59
Takarada T., Sato B., Omiya M., Hori Y., Fujii M. S., 2020, Radial-velocity search and statistical studies for short-period planets in the Pleiades open cluster (arXiv:2010.11577)
Trapman L., Rosotti G., Bosman A. D., Hogerheijde M. R., van Dishoeck E. F., 2020, A&A, 640, A5
Virtanen P., et al., 2020, Nature Methods, 17, 261
Wang Y.-H., Perna R., Leigh N. W. C., Shara M. M., 2022, MNRAS, 509, 5253
Weldrake D. T. F., Sackett P. D., Bridges T. J., Freeman K. C., 2005, ApJ, 620, 1043
Winter A. J., Alexander R., 2021, MNRAS,
Winter A. J., Clarke C. J., Rosotti G., Booth R. A., 2018a, MNRAS, 475, 2314
Winter A. J., Clarke C. J., Rosotti G., Ih J., Facchini S., Haworth T. J., 2018b, MNRAS, 478, 2700
Winter A. J., Kruijssen J. M. D., Longmore S. N., Chevance M., 2020, Nature, 586, 528
Winter A. J., Rosotti G. P., Clarke C., Giersz M., 2022, MNRAS, 509, 3924
Wright J. T., Marcy G. W., Howard A. W., Johnson J. A., Morton T. D., Fischer D. A., 2012, ApJ, 753, 160
Yee S. W., Tamayo D., Hadden S., Winn J. N., 2021, AJ, 162, 55

APPENDIX A: HYPERBOLIC PERTURBATION CROSS-SECTIONS

A1 Scaling of eccentricity perturbation

We are concerned with defining a cross-section for dynamical perturbations to an initial binary (star-planet system in this case) that result in a change of orbital eccentricity ϵ greater than some threshold $\epsilon_{\rm thr}$. Heggie & Rasio (1996) derived a general expression for ϵ under the influence of a hyperbolic encounter where the perturber with impact parameter $b_{\rm pert}$ has eccentricity:

$$e_{\rm pert} = \sqrt{1 + \frac{b_{\rm pert}^2 v_\infty^4}{G^2 m_{\rm tot}^2}}. \tag{A1}$$

Here the total mass of the three components is $m_{\rm tot} = m_*(1+q) + m_{\rm pert}$ and v_∞ is the relative speed of the perturber far from the barycentre. For the secondary (of mass qm_*) with position $\boldsymbol{r}$ with respect to the primary (of mass m_*), the eccentricity can be written:

$$\boldsymbol{e} = \frac{1}{Gm_*(1+q)}\dot{\boldsymbol{r}} \times (\boldsymbol{r} \times \dot{\boldsymbol{r}}) - \frac{\boldsymbol{r}}{r} \tag{A2}$$

The force of the perturbing star, separation $\boldsymbol{R}$ from the primary, on the initial binary can be written in spherical harmonic form:

$$\boldsymbol{F} = \frac{Gm_{\rm pert}}{R} \sum_{n=0}^{\infty} \frac{m_*^{n-1} - (-qm_*)^{n-1}}{[m_*(1+q)]^{n-1}} \nabla_r \left[\left(\frac{r}{R}\right)^n P_n\left(\frac{\boldsymbol{r}\cdot\boldsymbol{R}}{rR}\right)\right], \tag{A3}$$

where P_n is the $n^{\rm th}$ Legendre polynomial. The resulting acceleration of the secondary with respect to the primary is:

$$\ddot{\boldsymbol{r}} = -\frac{Gm_*(1+q)\boldsymbol{r}}{r^3} + \boldsymbol{F}, \tag{A4}$$

and the eccentricity changes as:

$$\dot{\boldsymbol{e}} = \frac{2(\boldsymbol{F}\cdot\dot{\boldsymbol{r}})\boldsymbol{r} - (\boldsymbol{r}\cdot\dot{\boldsymbol{r}})\boldsymbol{F} - (\boldsymbol{F}\cdot\boldsymbol{r})\dot{\boldsymbol{r}}}{Gm_*(1+q)}. \tag{A5}$$

In principle, equation A5 can now be integrated over time to give the change in eccentricity for a given perturber trajectory. In practice, this requires taking the lowest terms that do not vanish ($n = 2$, quadrupole) and making the assumptions that the encounter is tidal and slow (see discussion in Section A2). The approach for this is given by Heggie (1975) and again in Appendix A of Heggie & Rasio (1996), with a sign correction.

The resultant perturbation to eccentricity is necessarily dependent on all three of the usual orbital angles defining the orientation of the perturbers orbit with respect to the eccentric planet orbit. The line of nodes is the line of intersection of the orbital planes of the pertuber and the binary. The ascending node is then the point along this line where the perturber crosses the plane of the binary. The longitude of this ascending node Ω is defined in the sense of the binary angular momentum vector. The inclination between the two orbital planes is i, and ω be the longitude of pericentre of the third body, measured in its plane of motion from the ascending node, in the sense of its motion around the binary. With these definitions, for a binary with initial eccentricity e_0 the firsr order change in eccentricity is:

$$\epsilon \approx \alpha\, y\, a_0^{3/2} r_{\rm p}^{-3/2} \left\{\Theta_1(\Omega, i)\chi + [\Theta_2(\Omega, i, \omega) + \Theta_3(\Omega, i, \omega)]\,\psi\right\}, \tag{A6}$$

where we have defined:

$$y \equiv e_0\sqrt{1-e_0^2}\,\frac{m_{\rm pert}}{\sqrt{(1+q)m_* m_{\rm tot}}} \tag{A7}$$

and

$$\alpha = -\frac{15}{4}(1+e_{\rm pert})^{-3/2}, \qquad \chi = \underbrace{\arccos\left(\frac{-1}{e_{\rm pert}}\right)}_{\chi_1} + \underbrace{\sqrt{e_{\rm pert}^2 - 1}}_{\chi_2}, \qquad \psi = \frac{1}{3}\frac{(e_{\rm pert}^2-1)^{3/2}}{e_{\rm pert}^2}, \tag{A8}$$

and $r_{\rm p}$ is the closest approach distance. We have absorbed all of the dependence on orientation into the Θ_k:

$$\Theta_1 = \sin^2 i \sin 2\Omega, \qquad \Theta_2 = (1+\cos^2 i)\cos 2\omega \sin 2\Omega, \qquad \Theta_3 = 2\cos i \sin 2\omega \cos 2\Omega. \tag{A9}$$

This notation is convenient since each component Θ_k may vanish under particular assumptions about the orbit (e.g. $\Theta_{2,3}$ for a parabolic perturber orbit, Θ_1 for $i = 0°$, Θ_3 for $i = 90°$).

Converting equation A6 into a cross section can be approached in two ways. The approach of Heggie & Rasio (1996) is to find the domain $\mathcal{E}$ for which $\epsilon > 0$ (or equivalently < 0), then intergrate out to the maximum impact parameter $b_{\rm max}$ for which $|\epsilon| > \epsilon_{\rm pert}$. The case where the encounter is parabolic ($e_{\rm pert} \to 1$) is far simpler because $\psi = 0$ and the dependence on Θ_2 and Θ_3 (and therefore ω) is removed. The domain $\mathcal{E}$ in which ϵ is positive or negative is therefore trivially dependent on the sign of Θ_1, and the corresponding domain of Ω is simply $[\pi/2, \pi]$ and $[3\pi/2, 2\pi]$ for positive ϵ (and the complement for negative). In this case, the perturbation cross section can be easily written as equation 15, as established by Heggie & Rasio (1996).

However, this approach does not work if $e_{\rm pert} \neq 1$. In this case we must take a slightly different (numerical) approach. If we do not care

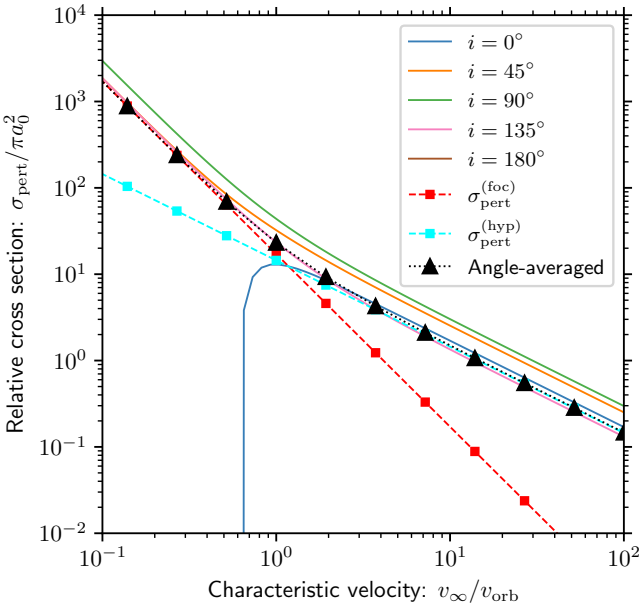

Figure A1. The cross section for perturbation, defined to be an interaction with $|\epsilon| > \epsilon_{\rm thr} = 0.05$, as a function of velocity of the perturber at infinity v_∞ normalised by the characteristic orbital speed $v_{\rm orb}$ of the planet. In all cases, the initial eccentricity is $e_0 = 0.9$ and the perturber mass $m_{\rm pert} = 0.5\,M_\odot = m_*$, the host star mass, while $q = 0$. We show results of numerical evaluations for specific orientations with fixed $\omega = \Omega = 15°$ and varying inclination i (the cross section vanishes for $i = 180°$). The angle averaged results calculated by numerically integrating equation A10 are shown by black triangles. The red squares show the corresponding cross sections in the gravitationally focused limit, as calculated by Heggie & Rasio (1996). The squares show the hyperbolic limit that we derive, with normalisation constant fitted to the angle averaged results.

about the sign of ϵ, then we are free to integrate over the full range of Ω, i, and ω; at each angle there exists some impact parameter $b_{\rm max}$ such that $|\epsilon| > \epsilon_{\rm thr}$ for $b_{\rm pert} < b_{\rm max}$ and $\epsilon_{\rm thr} > 0$. The cross section is then:

$$\sigma_{\rm pert} = \frac{1}{4\pi^2}\oint {\rm d}\Omega \oint {\rm d}\omega \oint {\rm d}i\ \frac{1}{2}\sin i \int_0^{b_{\rm max}(\Omega,i,\omega)} {\rm d}b\ 2\pi b = \frac{1}{4\pi}\int_0^{2\pi}{\rm d}\Omega \int_0^{2\pi}{\rm d}\omega \int_0^{\pi}{\rm d}i\ \sin i \cdot b_{\rm max}^2(\Omega,i,\omega). \tag{A10}$$

We then need to solve equation A6 for $b_{\rm max}$ more generally. Noting that

$$b_{\rm max}^2 = r_{\rm p,max}^2\left(1 + \frac{2Gm_{\rm tot}}{r_{\rm p,max}v_\infty^2}\right) \tag{A11}$$

for corresponding periastron distance $r_{\rm p,max}$, we write:

$$r_{\rm p,max}^{3/2} = a_0^{3/2}\epsilon_{\rm thr}^{-1} y \cdot |\alpha\left[\Theta_1\chi + (\Theta_2 + \Theta_3)\,\psi\right]|\,. \tag{A12}$$

The right hand side of equation A12 is valid because we allow positive or negative ϵ (i.e. $|\epsilon| > \epsilon_{\rm thr} > 0$). Here α, χ and ψ are dependent on $e_{\rm pert}$, which is in turn dependent on $r_{\rm p,max}$ (via equations A1 and A11). No analytic solution is forthcoming for $r_{\rm p,max}$, hence we solve equation A12 numerically across a range of v_∞ to give $r_{\rm p,max}$ across a grid in Ω, i, ω. We then integrate equation A10 numerically substituting in the upper limit $b_{\rm max}$ from equations A11 and A12.

The results of this exercise are shown in Figure A1 for our fiducial parameters ($a_0 = 5$ au, $e_0 = 0.9$, $m_{\rm p} = m_* = 0.5\,M_\odot$, $\epsilon_{\rm thr} = 0.05$). We have also adopted $q = 0$, the test particle limit, although this assumption would not significantly alter the results while $q \ll 1$. A number of features are require highlighting. Firstly, we consider the $i = 0°$ results (for $\omega = \Omega = 15°$), for which only the hyperbolic component contributes. In this case, we have $\Theta_1 = 0$ but $\Theta_{2,3} \neq 0$. This is in contrast to the general $e_{\rm pert} = 1$ case where $\psi = 0$ and hence Θ_2 and Θ_3 both effectively vanish. When $\psi \neq 0$, $\epsilon \propto a_0^{3/2} y r_{\rm p}^{-3/2} e_{\rm pert}^{-1/2} \propto a_0^{3/2} y r_{\rm p}^{-2} v_\infty^{-1} m_{\rm tot}^{1/2}$. Substituting these expressions back into equation A10, we have:

$$\sigma_{\rm pert}^{\rm (hyp)} \propto b_{\rm max}^2 \propto r_{\rm p,max}^2 \propto a_0^{3/2} y v_\infty^{-1} \epsilon_{\rm thr}^{-1} m_{\rm tot}^{1/2} \propto a_0^2 \cdot y \epsilon_{\rm thr}^{-1}\left(\frac{v_\infty}{v_{\rm orb}}\right)^{-1}\sqrt{1 + \frac{m_{\rm pert}}{m_*(1+q)}}, \tag{A13}$$

which is shallower in v_∞ than the focused version given by equation 15. Meanwhile, taking the ψ component for $e_{\rm pert} \to 1$ we have $\epsilon \propto y r_{\rm p}^{-3/2}(e_{\rm pert} - 1)$. Hence $r_{\rm p,max}$ vanishes for fixed $\epsilon_{\rm thr}$ as $v_\infty \to v_{\rm orb}$ for decreasing v_∞. In this case, it is possible that $|\epsilon|$ would in fact be dominated by the second order terms that apply to initially circular binaries (see Heggie & Rasio 1996). Since the contribution for $i = 0°$ is a special case that does not strongly influence our angle averaged result, we do not consider the second order terms here. Another special case where the first order terms vanish is $i = 180°$: $\Theta_1 = 0$ and $\Theta_2 = -\Theta_3$ when $\omega = \Omega$. Again, in this case second order terms must be computed, although this would not influence the angle averaged results.

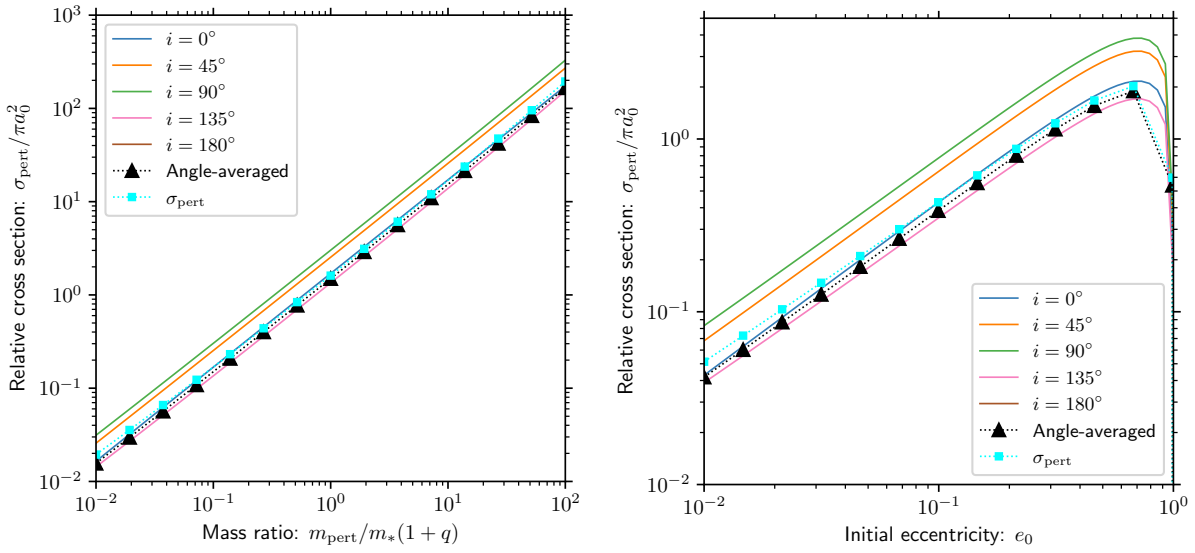

(a) (b)

Figure A2. As in Figure A1 except for fixed $v_\infty/v_{\rm orb} = 10$ and varying $m_{\rm pert}$ (Figure A2a) and e_0 (Figure A2b). Because $v_\infty/v_{\rm orb} \gg 1$ we are always in the hyperbolic limit, such that $\sigma_{\rm pert} \approx \sigma_{\rm pert}^{\rm (hyp)}$.

More generally, if $\Theta_1 \neq 0$ then as $e_{\rm pert} \to \infty$ we have $\chi \propto \psi$ such that $\epsilon \propto a_0^{3/2} y r_{\rm p}^{-2} v_\infty^{-1}$ as before. However, in the limit $e \to 1$ we have $\psi \to 0$ and $\chi_2 \to 0$, but in this case $\chi \to \chi_1 \to \pi$. We then have $\epsilon \propto a_0^{3/2} y r_{\rm p}^{-3/2}$ only – i.e. independent of v_∞. Then

$$\sigma_{\rm pert}^{\rm (foc)} \propto b_{\rm max}^2 \propto r_{\rm p,max} m_{\rm tot} v_\infty^{-2} \propto a_0 \epsilon^{-2/3} y^{2/3} m_{\rm tot} v_\infty^{-2} \propto a_0^2 \cdot \epsilon_{\rm thr}^{-2/3} y^{2/3} \left(\frac{v_\infty}{v_{\rm orb}}\right)^{-2} \left[1 + \frac{m_{\rm pert}}{m_*(1+q)}\right], \tag{A14}$$

as in equation 15. We can therefore write the ratio of the hyperbolic to focused cross section:

$$\Delta_{\rm hf} = \sigma_{\rm pert}^{\rm (hyp)}/\sigma_{\rm pert}^{\rm (foc)} = C_{\rm hf}\Delta'_{\rm hf} \propto a_0^{1/2} \epsilon_{\rm thr}^{-1/3} y^{1/3} m_{\rm tot}^{-1/2} v_\infty \propto \epsilon_{\rm thr}^{-1/3} y^{1/3} \frac{v_\infty}{v_{\rm orb}} \left[1 + \frac{m_{\rm pert}}{m_*(1+q)}\right]^{-1/2}, \tag{A15}$$

where $C_{\rm hf}$ is a constant which can be obtained by numerically computing the angle averaged cross section in the hyperbolic case. We therefore have a general encounter cross section:

$$\sigma_{\rm pert} = \sigma_{\rm pert}^{\rm (foc)} \left[1 + \Delta_{\rm hf} \frac{v_\infty}{v_{\rm orb}}\right] = \sigma_{\rm pert}^{\rm (foc)} \left\{1 + C_{\rm hf} y^{1/3} \epsilon_{\rm thr}{}^{-1/3} \left[1 + \frac{m_{\rm pert}}{m_*(1+q)}\right]^{-1/2} \frac{v_\infty}{v_{\rm orb}}\right\}, \tag{A16}$$

where $C_{\rm hf} \approx 0.67$ is a factor numerically computed from the angle averaged results (Figure A1) for our fiducial parameters: $e_0 = 0.9$, $a_0 = 5$ au, $m_{\rm pert} = m_* = 0.5\,M_\odot$, $q = 0$ and $\epsilon_{\rm thr} = 0.05$.

As a sanity check, we compare the equation A16 with the fitted constant $C_{\rm hf}$ to the numerical integrations with variable $m_{\rm pert}$ and e_0 in Figure A2 for the hyperbolic limit ($v_\infty/v_{\rm orb} = 10$). In both cases, we find good agreement between the analytic scaling and the numerical calculation. For variable $m_{\rm pert}$ (Figure A2a), we obtain the linear scaling with $m_{\rm pert}$ we expect because:

$$\sigma_{\rm pert}^{\rm (hyp)} \propto y\sqrt{1 + q_{\rm pert}} = e_0\sqrt{1 - e_0^2} q_{\rm pert}, \tag{A17}$$

where $q_{\rm pert} \equiv m_{\rm pert}/(1+q)m_*$. In the varying e_0 case, Figure A2b, the perturbation peaks at $e_0 = \sqrt{2}/2$. We conclude that equation A16 is a valid approximation for the effective perturbation cross section of an eccentric binary (or star-planet system).

A2 Applicability of the analytic cross section

The two primary assumptions made by Heggie & Rasio (1996, see also Heggie 1975) are that encounters are *tidal* and *slow*. The tidal condition is that the closest approach distance $r_{\rm p}$ of the perturber considerably exceeds the semi-major axis a_0. In the hyperbolic limit, we have $\sigma_{\rm pert} \approx \pi r_{\rm p}^2$ and therefore from equation 19 we require:

$$y\sqrt{1 + \frac{m_{\rm pert}}{m_*(1+q)}} \left(\frac{v_\infty}{v_{\rm orb}}\right)^{-1} \gg C_{\rm hyp}^{-1} \epsilon_{\rm thr}, \tag{A18}$$

where $C_{\rm hyp}$ is the constant factor for the RHS of equation A13 that turns the expression into an equality. The second requirement, that encounters are slow, is used to average over the binary (star-planet) orbit to obtain the change of eccentricity. This requires that the angular

velocity of the perturber at closest approach is slower than the angular velocity of the binary. In the hyperbolic limit, this is equivalent to the condition:

$$\sqrt{\frac{m_{\rm pert}}{m_{\rm tot}}\left(1+\frac{m_{\rm pert}}{m_*(1+q)}\right)}\frac{r_{\rm p}}{a_0} \gg \frac{v_\infty}{v_{\rm orb}}, \tag{A19}$$

or

$$y\frac{m_{\rm pert}}{m_{\rm tot}}\left(1+\frac{m_{\rm pert}}{m_*(1+q)}\right)^{3/2}\left(\frac{v_\infty}{v_{\rm orb}}\right)^{-3} \gg C_{\rm hyp}^{-1}\epsilon_{\rm thr}. \tag{A20}$$

The second of these expressions is more restrictive in our case where $v_\infty \gtrsim v_{\rm orb}$ and both are satisfied for sufficiently small $\epsilon_{\rm thr}$. In general we are interested in the many encounters that result in small changes in the eccentricity, such that we expect the approximations to hold. In either case, we are also never clearly in the fast encounter regime where the opposite of equation A19 applies. It is therefore not helpful to rework the cross sections in this limit (although see Section 3.2 and Appendix A4 of Heggie & Rasio 1996). In this work, we always adopt the slow encounter expressions.

APPENDIX B: STATISTICAL ECCENTRICITY EVOLUTION

In Appendix A we derived the general perturbation cross section for an encounter with a binary that yields a change of eccentricity of magnitude $\epsilon_{\rm thr}$. In the limit of small $\epsilon_{\rm thr} \to 0$, the time-scale for encounters $\tau_{\rm pert} \to 0$ and we are in the continuum limit of many distant encounters. In this case, we can model the evolution of the planet eccentricity e as a random walk. To do this, we first assume that for a small change τ from time t, the probability of a change eccentricity e_0 of magnitude greater than ϵ_0 is $\psi(e_0, \epsilon_0)$. For initial eccentricity within $\epsilon_0/2$ of e_0, the chance of having a new eccentricity $e > e_0$ where $e \in [e_1 - \epsilon_{\rm l}, e_1 + \epsilon_{\rm r}]$ where $\epsilon_{\rm l} = \epsilon_{\rm r} = \epsilon_1/2$ after time τ is therefore:

$$\epsilon_1 p_+(e_0; e_1, t+\tau) = \frac{\epsilon_0}{2}p(e_0,t)\left[\psi(e_0, e_1 - e_0 - \epsilon_{\rm l}) - \psi(e_0, e_1 - e_0 + \epsilon_{\rm r})\right], \tag{B1}$$

where the factor $1/2$ comes from the positive $\epsilon_{\rm thr}$ part of the cross section computed in Appendix A. In the limit of small $\epsilon_{\rm l}$ this becomes:

$$\epsilon_1 p_+(e_0; e_1, t+\tau) = -\frac{\epsilon_0\epsilon_1}{2}p(e_0,t)\partial_{(e_1-e_0)}\psi = \frac{\epsilon_0\epsilon_1}{2}p(e_0,t)|\partial_{e_0}\psi|. \tag{B2}$$

Considering also the probability density p_- of a planet being scattered away from the neighbourhood of e_1 and the probability density p_0 of it already occupying the neighbourhood without being scattered out, we have:

$$\epsilon_1 p(e_1, t+\tau) = \epsilon_1 p_0(\epsilon_1, t) - \epsilon_1 p_-(e_1, t) + \epsilon_1 \int_{\varepsilon} p_+(\tilde{e}; e_1, t)\,{\rm d}\tilde{e}, \tag{B3}$$

where ε is the complement of the local eccentricity space $\varepsilon = \overline{[e_1 - \epsilon_{\rm l}, e_1 + \epsilon_{\rm r}]}$. The probability of evacuating the enclosed region is:

$$\epsilon_1 p_-(e_1, t) = \epsilon_{\rm l} p(e_1, t)\psi(e_1, \epsilon_{\rm l}) + \epsilon_{\rm r} p(e_1, t)\psi(e_1, \epsilon_{\rm r}). \tag{B4}$$

The probability of having eccentricity within a small range ϵ of e is therefore:

$$\epsilon p(e, t+\tau) = \epsilon p(e,t)\left[1 - \frac{1}{2}\psi(e,\epsilon_{\rm l}) - \frac{1}{2}\psi(e,\epsilon_{\rm r})\right] + \frac{\epsilon_{\rm l}}{2}\int_0^{e-\epsilon_{\rm l}} p(\tilde{e},t)|\partial_{\tilde{e}}\psi(\tilde{e}, e-\tilde{e})|\,{\rm d}\tilde{e} + \frac{\epsilon_{\rm r}}{2}\int_{e+\epsilon_{\rm r}}^{1} p(\tilde{e},t)|\partial_{\tilde{e}}\psi(\tilde{e}, \tilde{e}-e)|\,{\rm d}\tilde{e}. \tag{B5}$$

We can then integrate the last terms by parts, noting that the sign of the derivative $\partial_{e_1-e_0}\psi$ changes sign for $e_0 < e_1$ and $e_0 > e_1$, as does the sign of the differential distance from e in the two integrals. However, this is not necessarily true for the derivative $\partial_{e_1-e_0}p$, hence the sign of the integral is changed above and below e. Finally, we must approximate the functional form of the probability ψ, which comes from the instantaneous rate $\Gamma(e, \epsilon)$ of pertubations to e greater than ϵ:

$$\psi(e,\epsilon) = 1 - \exp\left(-\int_0^\tau \Gamma(e,\epsilon){\rm d}t\right) \approx \Gamma\tau = \gamma e\sqrt{1-e^2}\frac{\tau}{\epsilon}, \tag{B6}$$

where we have used the hyperbolic perturbation rate computed in Section 2.4. In this case:

$$\Gamma \equiv \frac{\epsilon}{\tau} = \gamma e\sqrt{1-e^2}\epsilon^{-1}, \tag{B7}$$

such that equation 34 be written in terms of the drift diffusion equation with variable diffusivity:

$$\partial_t p(e,t) = \frac{\gamma}{2}\partial_e\left[e\sqrt{1-e^2}\partial_e p(e,t)\right] - \lim_{\epsilon\to 0}\left\{\Delta_- - \Delta_+\right\}. \tag{B8}$$

The last two terms are:

$$\Delta_- = \frac{\gamma}{2}\int_0^{e-\epsilon}\partial_{\tilde{e}}p(\tilde{e},t)\frac{\tilde{e}\sqrt{1-\tilde{e}^2}}{e-\tilde{e}}\,{\rm d}\tilde{e} \qquad \Delta_+ = \frac{\gamma}{2}\int_{e+\epsilon}^{1}\partial_{\tilde{e}}p(\tilde{e},t)\frac{\tilde{e}\sqrt{1-\tilde{e}^2}}{\tilde{e}-e}\,{\rm d}\tilde{e}, \tag{B9}$$

which are the drift terms. Both of these expressions appear to diverge as $\epsilon \to 0$. However, the two contributions actually cancel close to e. To show this, let us assume that $\Delta_\pm$ are both dominated by the contribution of the integrand close to e. Then as $\epsilon \to 0$, we consider a small region of size $\epsilon' \gg \epsilon$ around e over which we estimate the value of the integral by the midpoint approximation:

$$\Delta_- \approx \frac{\gamma}{2}\epsilon'\frac{\partial_e p(e-\epsilon'/2,t)\cdot(e-\epsilon'/2)\sqrt{1-(e-\epsilon'/2)^2}}{\epsilon'/2} \qquad \Delta_+ \approx \frac{\gamma}{2}\epsilon'\frac{\partial_e p(e+\epsilon'/2,t)\cdot(e+\epsilon'/2)\sqrt{1-(e+\epsilon'/2)^2}}{\epsilon'/2}. \tag{B10}$$

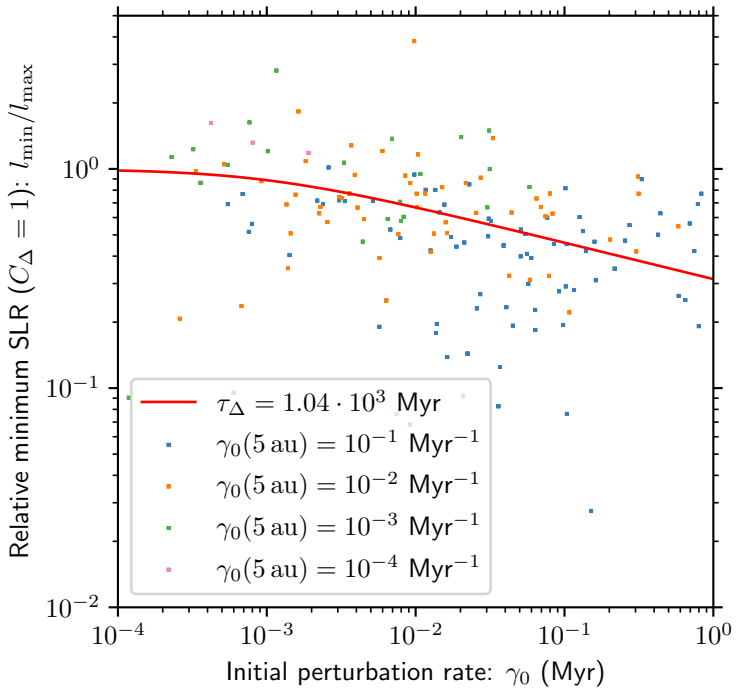

Figure C1. The distribution of the minimum semi-latus rectum (SLR, $l_{\rm min}$) distribution for planets that circularise during our fiducial random walk experiments ($e_0 = 1$) as a function of the initial perturbation rate γ_0. The ratio of the minimum SLR to the maximum value $l_{\rm max}$ predicted with the pre-factor $C_\Delta = 1$ is adopted. The red line shows the best fit assuming the functional form described by equation C2, with the fitting parameter $\tau_\Delta = 1.04 \cdot 10^3$ Myr.

Thus, if $p(e,t)$ is twice continuously differentiable at e we have:

$$\lim_{\epsilon' \to 0} \{\Delta_+ - \Delta_-\} \approx \gamma \epsilon' \partial_e \left[e\sqrt{1-e^2}\partial_e p(e,t) \right] \longrightarrow 0. \tag{B11}$$

We have therefore shown that the contribution of $\Delta_- - \Delta_+$ is finite as $\epsilon \to 0$. The PDE described by equation B8 can therefore be computed numerically.

APPENDIX C: RANDOM WALK CIRCULARISATION EXPERIMENTS

C1 Circularisation radii in the rapid encounter limit

During the analytic derivation of the maximum semi-latus rectum (SLR) along which a planet can circularise, we first assumed in Section 2.7 that we are able to ignore the non-local terms in the PDE (Δ in equation 34) that describes the statistical evolution of the planet eccentricity. However, this may not always be the case. In particular, for extreme eccentricities $e \to 1$, the diffusion coefficient that scales with $e\sqrt{1-e^2}$ becomes small. Thus if the minimum eccentricity $e_{\rm min}$ required for a planet to circularise (equation 48) is sufficiently large, then individual encounters that result in comparatively large changes in e – i.e. $|\epsilon| \gg 1 - e_{\rm min}$ – can dominate for circularising planets over many weak encounters. In this appendix, we will refer to encounters with a change of eccentricity $|\epsilon| \gg 1 - e_{\rm min}$ as 'strong' encounters, while $|\epsilon| \lesssim 1 - e_{\rm min}$ are 'weak' encounters. In the strong encounter regime, we must apply a correction factor for the contribution of these encounters in producing circularising planets.

Our approach for quantifying this correction factor is semi-empirical. We reason that the factor is $C_\Delta = 1$ for the weak encounter regime. In this case, strong encounters rarely yield circularisation outcomes because $e_{\rm min}\sqrt{1-e_{\rm min}^2}$ remains large. By contrast, when encounter rates are frequent, the required $e_{\rm min}\sqrt{1-e_{\rm min}^2}$ for circularisation becomes small. In the latter case, strong encounters may not be followed by sufficient numbers of weak encounters to influence the final circularisation radius. Thus the maximumum SLR (SLR, $l_{\rm max}$) scales more steeply with the initial encounter rate γ_0 than suggested by equation 47. From the governing PDE, equation 34, when the diffusion coefficient $D \propto \gamma e\sqrt{1-e^2}$ (equation 38) becomes small then the additional term $\Delta \cdot \gamma/2$ additionally contributes to the rate of eccentricity evolution. This non-local term becomes important when:

$$\gamma \frac{e_{\rm min}\sqrt{1-e_{\rm min}^2}}{1-e_{\rm min}} \gtrsim \tau_{\rm circ}^{-1}, \tag{C1}$$

where $\tau_{\rm circ}$ is defined at semi-latus rectum $l_{\rm max}$ and corresponding eccentricity $e_{\rm min}$. In general, we have $l_{\rm max} \propto 1 - e_{\rm min}^2 \approx 2(1 - e_{\rm min})$,

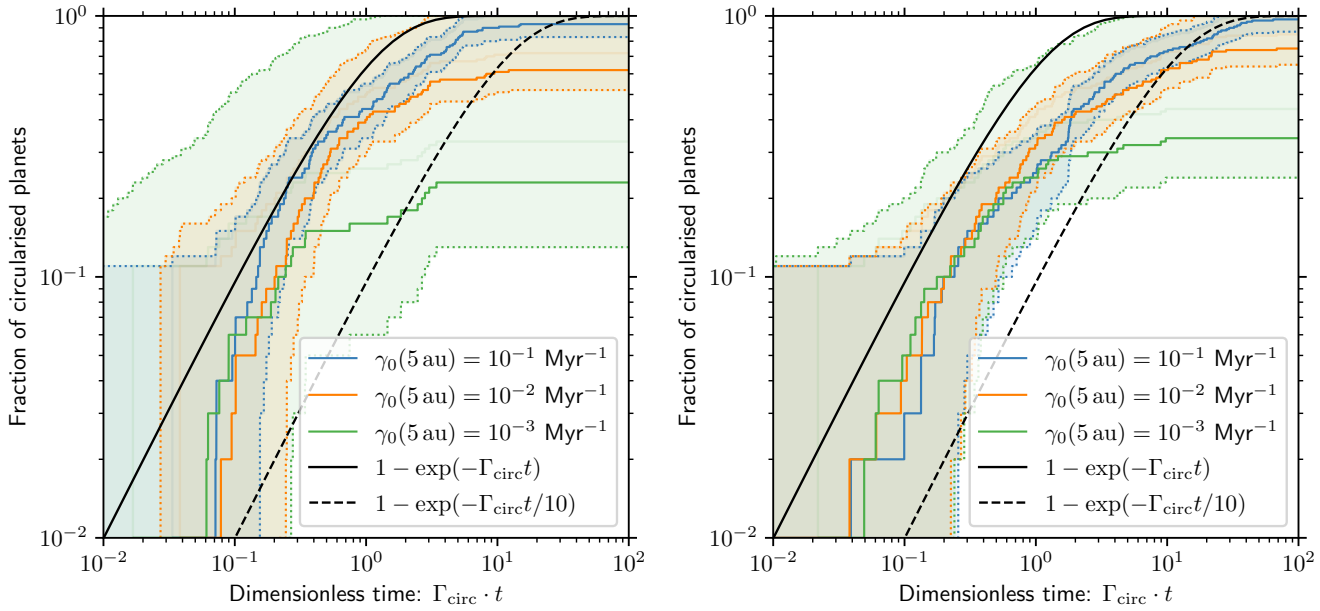

(a) $e_0 = 0.1$ (b) $e_0 = 0.6$ au

Figure C2. Distribution of the circularisation times obtained from random walk experiments with initial eccentricities $e_0 = 0.1$ (Figure C2a) and $e_0 = 0.6$ (Figure C2b). The time coordinate is mutliplied by $\Gamma_{\rm circ}$ as approximated by equation C3, which is the rate at which circularisation outcomes occur due to a single encounter. The solid black line shows the expected circularisation fraction if the true rate is $\Gamma_{\rm circ}$, while the dashed line shows the equivalent fraction if the rate is $\Gamma_{\rm circ}/10$. Circularisation over long time-scales is limited by the the integration time of our simulation, which is 10 Gyr. This contributes to the statistical uncertainties in the fraction of circularised planets, which are shown as shaded regions.

which is thus only weakly dependent on the local encounter rate (equation 47). Hence the relative importance of the non-local term is $\propto \tau_{\rm circ}\gamma$ in the rapid encounter rate limit. We thus estimate the correction factor:

$$C_\Delta \approx [1 + \tau_\Delta \gamma_0]^{-1}\,, \tag{C2}$$

where τ_Δ represents a constant time-scale that is an empirical fitting parameter. The second term on the RHS of equation C2 scales with γ_0 as $e_{\rm min} \to 1$ and the non-local terms dominate the encounter rate, while it remains of order unity for moderate $e_{\rm min}$.

In Figure C1 we show the outcome of the circularisation experiments we present in Section 2.8. Specifically, we show the minimum SLR $l_{\rm min}$ achieved by each planet undergoing a random eccentricity walk and subject to tidal forces. We normalise each $l_{\rm min}$ by the maximum SLR $l_{\rm max}$ predicted by equation 47 with $C_\Delta = 1$. We then consider this ratio as a function of γ_0, and fit an appropriate value for τ_Δ in equation C2 using the SciPy (Virtanen et al. 2020) package `optimize.minimize`. We obtain $\tau_\Delta = 1.04 \cdot 10^3$ Myr, which appears to reproduce the suppression in $l_{\rm max}$ at extreme γ_0 values (Figure C1). We therefore adopt the corresponding definition of C_Δ.

C2 Circularisation time-scale and eccentricity dependence

We are interested in understanding how the typical time-scale required for circularisation depends on the initial eccentricity of the planet e_0. To do this, we first make an analytic estimate of the expected rate at which planet circularise due to dynamical perturbations. To first order, we adopt the single-encounter approximation:

$$\Gamma_{\rm circ} \approx \frac{\gamma_0 e_0 \sqrt{1 - e_0^2}}{2\,(e_{\rm min} - e_0)}, \tag{C3}$$

which is equivalent to the $\Gamma^{\rm (hyp)}_{\rm pert}/2$ with $\epsilon_{\rm thr} = e_{\rm min} - e_0$ from equation 29. This is not an exact rate at which circularisation is instigated for a perturbed planetary systems because we assume that a single large encounter produces the required change in eccentricity. We thus ignore the many smaller encounters that result in a random walk in eccentricity that may increase or reduce the circularisation time-scale.

In Figure C2a we show the fraction of circularised planets from our numerical experiments presented in Section 2.8, with initial eccentricity $e_0 = 0.1$. In addition, we show the same experiment with an initial eccentricity $e_0 = 0.6$ in Figure C2b. We normalise the time coordinate by multiplying by $\Gamma_{\rm circ}$. We can then show the expected fraction of circularised planets:

$$P_{\rm circ} = 1 - \exp(-\Gamma_{\rm circ} t) \tag{C4}$$

as a solid black line in Figure C2. We find that the distribution of normalised circularisation time-scales is similar for both $e_0 = 0.1$ and $e_0 = 0.6$. For planets that circularise in time $\Gamma_{\rm circ} t \sim 0.1$–$1$, both distributions are well-described by equation C4. However, the distribution

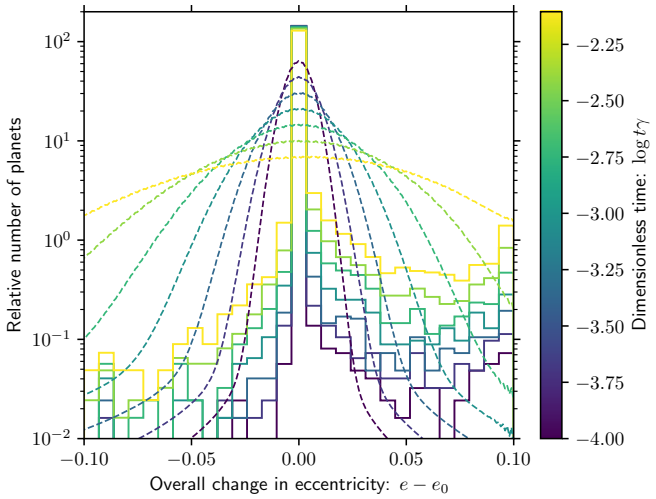

Figure D1. Statistical distribution of the orbital eccentricities for planets evolving in our dynamical model of 47 Tuc. The solid histograms are obtained directly from the results of Fewbody, implemented within the Mocca code. The dashed lines are the solution of the PDE described by equation B8. The colour bar shows the time evolution normalised by the encounter rate γ.

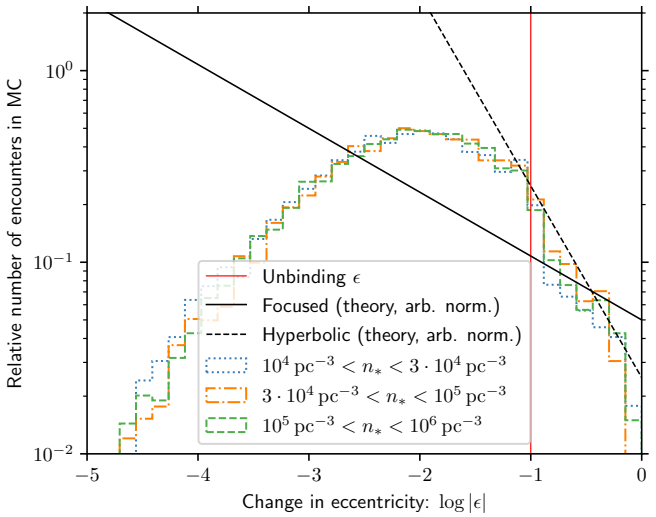

Figure D2. Histogram of the relative number of encounters that change a planets eccentricity by $|\epsilon|$ during our Mocca simulation, binned by initial local stellar density. We include only encounters that do not unbind the planet. For changes in eccentricity $|\epsilon| > 0.1$ (vertical red line) we apply a weighting of 2 because only encounters with a negative ϵ are possible. The two black lines show the theoretical distribution for focused encounters (solid line) and hyperbolic encounters (dashed line).

deviates from this expectation at the extreme ends of the distribution. For large $\Gamma_{\rm circ}t$, we are limited by the integration time-scale (10 Gyr). The fraction of planets that circularise at early times is limited by the initial time-step (0.1 Myr). In general, the true value of $\Gamma_{\rm circ}$ is well approximated by equation C3 within the uncertainties in our random walk experiments.

APPENDIX D: ANALYTIC ESTIMATE VS. FEWBODY

Here we compare the rate at which eccentric planets are perturbed in the Monte Carlo model using the Fewbody code with the theoretical eccentricity evolution. To achieve this we normalise the time coordinate in both cases by the characteristic time-scale γ^{-1}, where γ is defined in equation 35. In the case of the Monte Carlo simulation, γ is tracked at 100 Myr time intervals, such that the time-coordinate is in fact the estimated integral sum of $\gamma\Delta t$. We then compute the distribution of eccentricities expected following equation B8, for an initial eccentricity dispersion $\sigma_{e,0} = 10^{-3}$ around $e_0 = 0.9$.

The two distributions are compared in Figure D1. We generally see poor agreement between the two prescriptions. This is expected, and is a consequence of the algorithm used to compute encounters in Mocca. In the first instance, the prescription is designed to capture the physics of energy transfer, which influences the dynamical evolution of the cluster, rather than the evolution of the orbital eccentricity.

Because energy transfer drops exponentially with periastron distance r_p, the maximum closest approach R_{enc} can be limited to consider only encounters within a comparatively small radius $R_{enc} = X \cdot a$, where $X > 1$ is some factor and a is the semi-major axis of the binary (star-planet system in this case). In producing Figure D1 we have adopted $X = 2$, which results in many encounters that yield eccentricity changes $|\epsilon| \lesssim 0.05$ to be ignored. This can be seen in the evolution of the distribution of the orbital eccentricities, where at early times the fraction of systems which have $e - e_0 \gtrsim 0.05$ are much better produced than those with smaller changes in the Monte Carlo model.

Unfortunately, increasing the value of X is not a solution to this problem. When X becomes large, the number of encounters that occur on a single time-step also becomes large. In the Mocca framework, the large number of small encounters is replaced with a single close encounter, drawn from the appropriate distribution in relative velocity and closest approach distance. This is acceptable for energy transfer, but not for computing the orbital eccentricity evolution. In principle one could decrease the time-step, however this would ultimately undermine the purpose of the Monte Carlo prescription and quickly become computationally impracticable. In the limit of large X, this would also replicate something similar to the experiment by Hamers & Tremaine (2017), with no benefit in terms of the parameter space exploration.

We can however extract some quantitative comparison between the theoretical prediction and Monte Carlo results. This comparison is the relative number of encounters that result in a change of eccentricity of size $|\epsilon|$. This distribution (in log space) is shown in Figure D2. For hyperbolic encounters we expect the relative number of encounters to scale with $|\epsilon|^{-2}$. This is what we find for sufficiently large eccentricity ($|\epsilon| \gtrsim 0.05$) within the Monte Carlo model, independently of the local stellar density. While we are unable to directly compare the Monte Carlo and theoretical predictions for the eccentricity evolution, this exercise somewhat justifies our prescription. A further benchmarking exercise is performed in Section 2.11.2, where we compare to the more accurate numerical experiments by Hamers & Tremaine (2017).

This paper has been typeset from a TEX/LATEX file prepared by the author.